Controlling reduction degree of graphene oxide-based electrode for improving the sensing performance toward heavy metal ions

Published: 06 February 2021

Volume 127, article number 170, (2021) Cite this article

Applied Physics A

Aims and scope

Submit manuscript

Theeazen AL-Gahouari, Pasha Sayyad, Gajanan Bodkhe, Nikesh Ingle, Manasi Mahadik, Sumedh Shirsat & Mahendra Shirsat

Abstract

The influences of electrochemical reduction degrees of reduced graphene oxide (rGO)-based electrode on its electrochemical sensing performance toward heavy metal ions (HMIs) were investigated. Initially, graphene oxide was synthesized by the modified Hummers' method. Then, rGO films with different degrees of electrochemical reduction were prepared by using the cyclic voltammetry (CV) technique in different numbers of voltammetric cycles x (where $x = 3$, 6, 9, and 12). The structural and morphological characterizations of different degrees of reduction for rGOx were carried out by using ultraviolet–visible spectroscopy, attenuated total reflection-infrared, X-ray diffraction, atomic force microscopy, field emission scanning electron microscopy, and energy-dispersive X-ray spectroscopy.

The charge transfer rate of rGOx modified glassy carbon electrodes (rGOx/GCEs) was investigated by CV and electrical impedance spectroscopy measurements using a standard ferri/ferrocyanide system. These modified electrodes were further investigated to achieve the best electrochemical performance toward HMIs detection. The modified electrode with six voltammetric cycles (rGO6/GCE) exhibited considerable improvements related to the stability, sensitivity, and well-oxidation potential definition for cadmium ion (Cd^{2+}) and lead ion (Pb^{2+}). The deposition potential, pH value, and accumulation time were optimized. The simultaneous electrochemical detection of Cd^{2+} and Pb^{2+} was performed using differential anodic stripping voltammetry technique under optimized conditions in the presence of bismuth ion (Bi^{3+}). The Bi/rGO6/GCE was selected as the desired electrode and employed to detect the Cd^{2+} and Pb^{2+} at different concentrations within a linear range between 10 and 50 μgL^{-1}. The detection limits for Cd^{2+} and Pb^{2+} were 1.2 and 0.2 μgL^{-1}, respectively; with a signal to noise ratio (S/N = 3). Finally, the repeatability and reproducibility were investigated which exhibited excellent stability with relative standard deviations equal to 2.9 and 0.7% for Cd^{2+} and Pb^{2+} respectively, and similar linear range with detection limits.

Graphic abstract

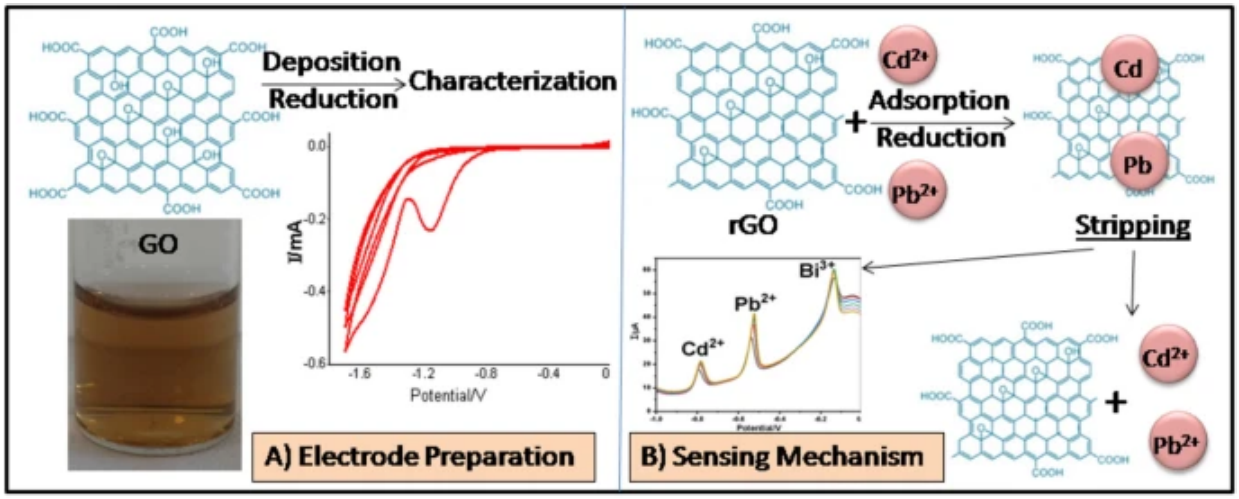

Similar content being viewed by others

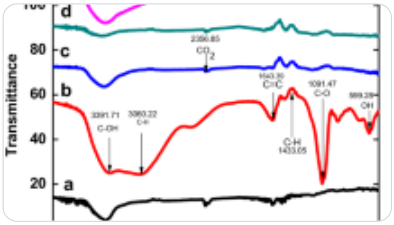

The comparative analyses of reduced graphene oxide (RGO) prepared via green, mild and chemical...

Article | 07 September 2019

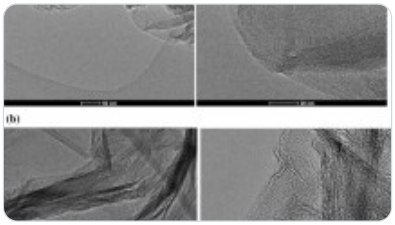

Chemical and structural properties of reduced graphene oxide—dependence on the reduci...

Article | Open access
09 November 2020

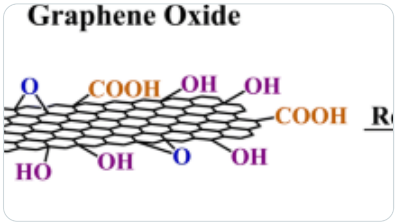

Thermally reduced graphene oxide: synthesis, studies and characterization

Article | 30 May 2018

1 Introduction

Nowadays, access to freshwater has become the ultimate goal for the environmental research community due to the developments in the anthropic actives which affect freshwater sources in direct and indirect ways. Among these activates, electroplating, fabrication of batteries, mining, and microelectronics are considered as the main water pollution sources with heavy metal ions (HMIs). The term HMIs is generally referred to as any metal with five times greater density than that of water, at least. The disadvantages accompanied by them, such as non-biodegradable and migration ability make them a cause of concern. Therefore, in case they entered into the human body with water or food, they can easily migrate and accumulate in the body, leading to a disturbance in the metabolism processes. However, some of these metals such as Zn^{2+}, Cu^{2+}, Co^{2+}, Mn^{2+}, Mo^{6+}, and Fe^{3+} are vital for metabolism maintenance. Still, unfortunately, they will be toxic when exceeding trace levels [1–3].

Moreover, there are some HMIs that are very toxic at low concentration levels with no known benefits, such as Hg^{2+}, Cd^{2+}, Pb^{2+}, and As^{3+}. Diseases produce from HMIs depend on different factors like the type of metal ion, its concentration, and the exposure period. For example, Hg^{2+} and Pb^{2+} negatively affect the nervous system, Cd^{2+} causes kidney diseases, etc. The toxicity levels of these metals in the drinking water were identified by many agencies, such as the world health organization (WHO), which assigned for Pb^{2+}, Cd^{2+}, and Hg^{2+} to be 10, 3, and 2 μgL^{-1}, respectively [4]. Therefore, an efficient methodology for the detection and removal of these HMIs needs to be developed.

Different methods and techniques have been developed for the trace of toxic metals determination such as atomic absorption spectrometry (AAS) [5], electro-thermal atomic absorption spectrometry (ETAAS) [6], flame atomic absorption spectrometry (FAAS) [7], inductively coupled plasma-atomic emission spectrometry (ICP-AES) [8], inductively coupled plasma-mass spectrometry (ICP-MS) [9], and inductively coupled plasma optical emission spectrometry (ICP-OES) [10]. However, these methods are expensive to run, require professional maintenance and sophisticated instrumentation and skilled personnel [11–13]. Despite the disadvantages of traditional techniques, electrochemical stripping analysis has been recognized as a powerful technique for tracing these metals. Due to its remarkable sensitivity, ability for multi-element determination, relatively inexpensive instrumentation, and capacity to determine elements at trace and ultra-trace levels, the electrochemical technique has been preferred [13].

Usually, the accumulation and stripping of metals in electrochemical techniques occur at a specific electrode called a working electrode. Traditional hanging mercury drop (HMD) electrodes are considered the most capable electrodes for the sensitive and selective detection of HMIs. However, due to its toxicity impact, environment-friendly electrodes have replaced it; bismuth film is one of them [14]. Usually, the drawbacks in the electrochemical sensor lie in its small effective area of the working electrode. Thus it is necessary to solve this problem by choosing such a technique and material to improve the working electrode's surface area. However, when the surface area concept has been highlighted, nanotechnology becomes the best option for surface area improvement. However, this option requires such materials, which will have novel properties like excellent conductivity, enough porosity, cost-efficiency, good stability, environmental safety, easy configurative, etc. Among these materials, carbon nanomaterials have been dominant in this field, especially carbon nanotubes and graphene [15–26].

Graphene has been highlighted as a novel material owing to the one-atom thickness structure, large specific surface area, high flexibility, high electrical and thermal conductivity, and exceptional mechanical and optical properties. Thereby, it has been integrated into novel sensor applications with additional improvements regarding a small device size, low energy consumption, fast response, and a user-friendly analytical platform [27–33]. The mechanisms by which graphene and its derivatives respond to toxic HMIs are adsorption and ion-exchange mechanisms [34–36]. The ion-exchange mechanism between graphene derivatives and HMIs occurs due to the electrostatic interaction between rich negative oxygen-containing functional group density on its structure and positive metal ions in the solution. The adsorption mechanism occurs due to the active vacant sites on the large honeycomb surface area of the graphene structure for HMIs in solution [37–39]. Many systematic approaches have been explored to produce graphene, such as thermal, electrochemical, mechanical, and chemical approaches. These approaches have advantages and disadvantages in scalability, controllability,

defectives, conductivity, and large mass production [40]. For large mass production and controlling the synthesizing of graphene, the chemical approach has been widely used. The synthesis of graphene by the chemical method can be achieved in two steps. The first step is to insert many oxygen-containing functional groups between graphite layers using strong oxidized agents to produce graphene oxide (GO). The second step is by introducing the GO to the reduced reagents or other reduction methods [41]. Hence, the GO considers as a raw material for synthesizing graphene by chemical method. However, usually, the reduction process of graphite oxide does not totally remove the oxygen-containing functional groups from graphite oxide sheets; in this way, referring to this resultant as reduced graphene oxide (rGO). Therefore, the fluctuations in the degree of reduction of rGO directly affect its properties [42].

A few articles have concerned about the impact of the reduction degree of rGO on the sensor application. For example, Daniela et al. examined the sensitivity influences of the nucleic acid biosensor by four different types of rGO-based electrodes which were reduced by four different methods (i.e., chemical, hydrothermal, electrochemical, and thermal). The conclusion was that the thermally rGO-based electrode produced the best electrochemical performance due to the higher polydispersity and smaller sheet size which led to high defects on the electrode surface and this resulted in enlarging its surface area [43]. Cherukutty et al. studied the detection of ammonia and toluene at room temperature by using three types of rGO-based electrode, which were reduced by hydrazine in three different periods. The desired electrode was with a long reduction period, which is justified by its reproducibility due to creating new defects that have replaced the oxygen-containing functional groups after a long period of thermally rGO [44]. Chen et al. studied relative humidity sensitivity at different thermal reduction degrees of rGO. The result referred that the sensitivity toward the humidity increases while the thermal reduction degrees increase [45].

To the best of our knowledge, numerous articles related to electrochemical sensors based on graphene and its related materials have been published, no single article has been published which illustrates the influence in the degree of reduction of rGO on the sensitivity, stability, and performance of an electrochemical sensor toward HMIs. Moreover, the electrochemical detection of the HMIs depends not only on the electrode's electrochemical conductivity, but also on the amount and type of chelating ligands on this material's surface [46]. Therefore, the oxygen-containing functional groups on the rGO surface have been employed as chelating ligands to capture the HMIs from aqueous media [47]. Nevertheless, there are different binding strength degrees of the oxygen-containing functional groups on the rGO surface due to their type and location, which directly impact the stability and sensitivity of the electrochemical sensor toward HMIs detection. Hence, it may be worthwhile to study the degree of reduction of the rGO to obtain the desired response signal for HMIs detection.

The present investigations suggest a green and straightforward approach to achieve the best performance of rGO-based electrode to detect HMIs by selecting the desired electrochemical reduction degree of rGO which is considered as an essential step for optimizing the experimental condition. Here, a fast and straightforward approach for the preparation of different reduction degrees of rGO-based electrode by electrochemical method from GO has been employed. The rGO modified glassy carbon electrodes (GCEs) have been utilized for simultaneous detection of Cd^{2+} and Pb^{2+} using differential pulse anodic stripping voltammetry (DPASV). Bismuth has been introduced to the supporting electrolyte for better resolution achievement of HMIs stripping signals due to its good fused alloy formation and less susceptible to oxygen background interference. The structural, morphological, and electrochemical behavior of different reduction degrees of rGO was investigated. The sensing results show the ability of rGO/GCE at the desired degree of reduction to detect the HMIs under toxic level determined by WHO with excellent stability.

2 Experimental work

2.1 Reagents and apparatus

Graphite powder extra pure (60 mesh), KCl, and $K_3Fe(CN)_6$ were bought from Sigma Aldrich. The working solution containing Cd^{2+}, Pb^{2+}, and Bi^{3+} that were prepared from respective metal salts. A supporting electrolyte was prepared from a 0.1 M of acetate buffer (HAc-NaAc) solutions by mixing appropriate quantities of (CH_3COOH, CH_3COONa). Different values of pH were adjusted by adding appropriate quantities of 0.1 M of HCl and 0.1 M of NaOH. A CHI660C electrochemical workstation performed the electrochemical measurements. The field emission scanning electron microscopy (FESEM) attached with energy-dispersive X-ray spectroscopy (EDX) and non-contact mode atomic force microscopy (AFM) were used to examine the surface morphology which was performed using a Model JSM-6160 microscope and Park Systems; XE-7, respectively. Structural fingerprints were investigated by Raman spectrum; AIRIX corp STR150 model, ultraviolet–visible (UV–vis) spectroscopy; (JASCO V-750), attenuated total reflection infrared (ATR-IR) and X-ray diffraction XRD (advance 8 Broker). All the aqueous solutions were prepared with extra pure DI.

2.2 Preparation of GO dispersion

The precursor GO dispersion was synthesized based on the modified Hummers' method from thermally expanded graphite powder; detailed procedures presented in (supplementary information) S1.1 [48–52]. For preparing GO stock solution with 3 $mgmL^{-1}$ concentrations, the as-prepared graphite oxide powder was dispersed in DI water and ultrasonicated for 40 min followed by centrifugation treatments to remove unexfoliated graphite oxide sheets. Again, 5 mL of 0.1 $mgmL^{-1}$ GO solution was prepared by diluting from the stock solution and ultrasonicated for 15 min to give a cleared

transparency yellowish GO solution as shown in (supplementary information) Figure S1.2.

2.3 Preparation of modified electrodes

Three types of substrates have been chosen to perform this work, namely ITO, copper clad, and GCE. In contrast, the ITO and copper-clad were modified with the GO and rGO films used for morphological, structural, and spectral characterization, respectively. The modified GCEs were used for electrochemical characterizations and sensing experiments.

For preparing GO/cupper clad films, five pre-cleaned copper-clad substrates were spin-coated independently with 40 µL of 3 $mgmL^{-1}$ GO stock solution for 30 s at 2000 rpm. Also, five GO/ITO films were prepared by drop-casting of 20 µL of 0.1 $mgmL^{-1}$ GO solution on the pre-cleaned ITO substrates, independently. Finally, the preparation of GCE modified by GO was done by drop-casting of 5 µL of 0.1 $mgmL^{-1}$ GO solution on the pre-cleaned GCE. This process was repeated to obtain five electrodes. All these 15 electrodes were kept in a desiccator under N_2 ambient for 24 h inside an oven at 40 °C.

2.3.1 Procedure for electrochemical testing

The electrochemical tests were carried out on the electrochemical workstation with an electrochemical cell contains 50 mL quartz beaker capacity and three electrodes. These three electrodes assigned as a modified electrode (GCE, ITO, and copper-clad), platinum plate, and saturated calomel electrode (SCE) were used as a working, counter, and reference electrode. A 50 mL of 0.1 M acetate buffer (HAc−NaAc) solution with pH 4.5 was used as a supporting electrolyte. For the DPASV analyses, the GCE modified electrodes were immersed into the electrolyte containing 500 μgL^{-1} Bi^{3+} and other HMIs under vigorous stirring to get an abundant concentration of HMIs around the effective active area of modified GCE. The charge-transfer rate was performed by cyclic voltammetry (CV) and electrical impedance spectroscopy (EIS) techniques, respectively, in a 0.1 M KCl solution contained 5 mM of $[Fe(CN)_6]^{3-/4-}$ [53, 54].

2.3.2 Electrochemical reduction of modified electrodes.

The CV technique can electrochemically reduce the GO by repeating the sweeping cycles within an appropriate potential range [55–57]. Therefore, as-prepared GO modified electrodes were immersed in the supporting electrolyte solution and electrochemically reduced by CV technique with a scan rate of 50 mV/s in the range between 0 and - 1.7 V; with the negative initial scan polarity. For obtaining the modified electrodes with different electrochemical reduction degrees, each type of the three types of GO modified electrodes (i.e., GO/GCEs, GO/ITO, and GO/cupper clad electrodes) was electrochemically reduced by 0, 3, 6, 9, and 12 numbers of voltammetric cycles to produce five different electrodes in each type of electrode. All these modified electrodes were kept in the desiccator with N_2 ambient at 40 °C for

24 h. For preparing free-stand film samples, the copper-clad modified electrodes were immersed in acetone solution for 10 min, followed by drying in a vacuumed dissector which kept in the oven at 50 °C for 12 h. The GO and rGO films with different electrochemical reduction degrees have been peeled easily from the copper-clad surface. Finally, the rGO samples with different electrochemical reduction degrees were obtained and respectively marked as rGOx, where x indicated the number of reduction voltammetric cycles (x = 3, 6, 9, and 12).

3 Result and discussions

3.1 Spectroscopic characterizations

3.1.1 ATR-IR spectroscopy study

ATR-IR spectroscopy was used to represent the degree of removing the oxygen-containing functional groups from the graphene oxide sheets with different electrochemical reduction degrees [57]. Figure 1 shows the ATR-IR transmittance spectra for free-standing films of GO, rGO3, rGO6, rGO9, and rGO12, respectively (from down to up). The spectra illustrate five typical absorption bands at 2860−3420, 1710, 1622, 1340, and 1028 cm^{-1} corresponding to the bending vibration and stretching of −OH, vibration and stretching of carbonyl C = O, O−H bending and aromatic C = C stretch, epoxy and alkoxy C−O stretch groups, respectively. The significant changes in absorption peaks in these spectra have been observed at −OH stretch groups due to its weak binding within non-covalent interaction between it and the basal plane of GO sheets leading to removal easily. Moreover, the inset in Fig. 1 shows the extensive removal of −OH groups at the rGO3. It decreases behind that confirming the weak binding of hydroxyl groups, which are easy to remove in the first beginning electrochemical reduction cycles. The remaining hydroxyl functional groups did not show any appreciable changes which might be explained in terms of the locations of these groups on the edges and defects of GO sheets due to a strong binding with them [55, 58, 59].

Fig. 1

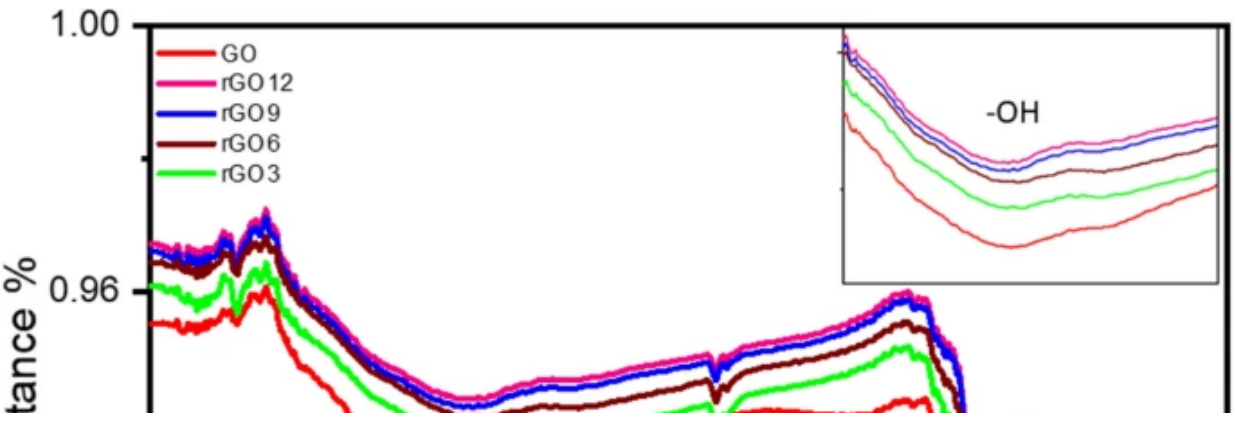

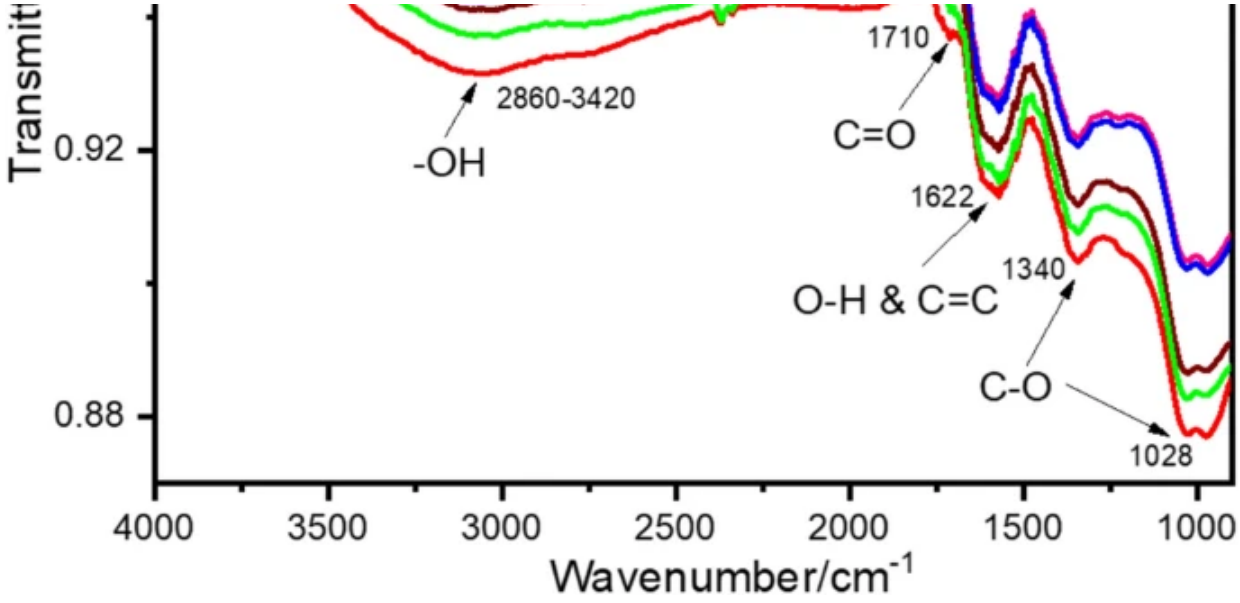

ATR-IR spectra of GO, rGO3, rGO6, rGO9, and rGO12

3.1.2 UV–vis spectroscopy study

The UV–vis spectroscopy samples were prepared by the same concentrations of GO, rGO3, rGO6, rGO9, and rGO12 dispersion in ethylene glycol with a ratio of 0.2 $mgmL^{-1}$ by ultrasonication for 0.5 h. The large particles were separated using centrifugation for 8 min at 700 rpm. Figure 2 shows the UV–vis absorption spectra of GO, rGO3, rGO6, rGO9, and rGO12. UV-vis spectroscopic measurements of GO dispersion exhibit a strong absorption peak at 232 nm assigned for $\pi \rightarrow \pi^*$ transition bonding of C=C aromatic rings, a shoulder peak at 302 nm resulting from $n \rightarrow \pi^*$ transition of C=O bonds [49, 60]. While the electrochemical reduction process, this strong absorption peak at 232 nm red-shifted to 234, 245, 249, and 264 nm for rGO3, rGO6, rGO9, and rGO12, respectively. This red-shifting indicated that the structure restoring of graphene due to the removal of oxygen from oxygen-containing functional groups during the electrochemical reduction processes led to the easy transfer through π-network in the aromatic structure of rGO [49, 61]. However, this absorption peak gradually decreases with increasing electrochemical reduction degree, indicating that the part of rGO precipitated gradually after centrifugation due to the graphene's hydrophobic nature [62]. The shoulder peak at 302 nm remains in a fixed position at all UV–vis spectra, confirming that the bonding of C=O is strong enough to sustain under the electrochemical reduction processes without any appreciable changes due to its location on the edges and defects of GO sheets[63]. These results exhibit excellent support to that in ATR-IR, where the appreciated changes were in the –OH functional group represented by $\pi \rightarrow \pi^*$ transitions and low changes were in the C=O functional group represented by $n \rightarrow \pi^*$ transitions.

Fig. 2

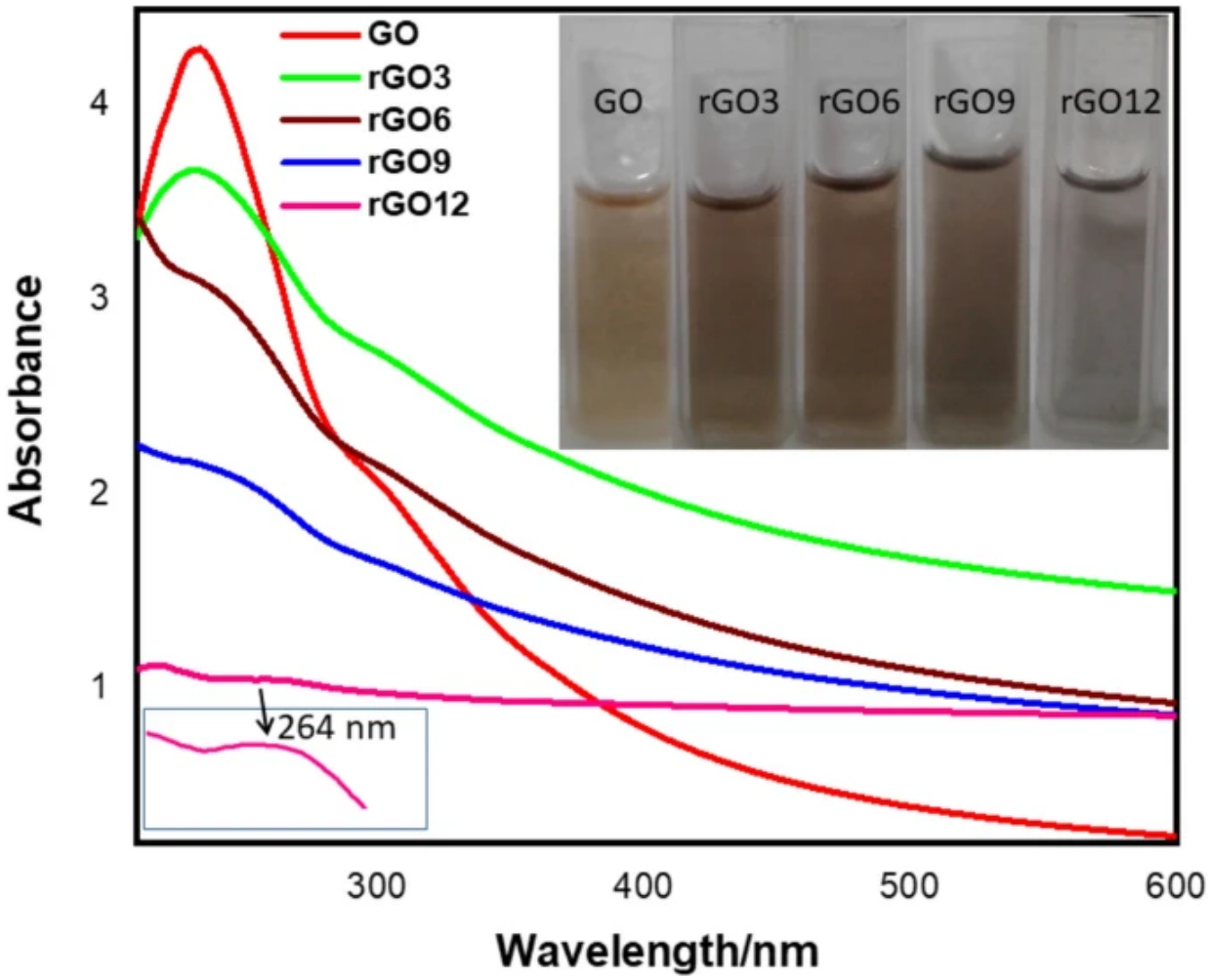

UV–Vis spectra of GO, rGO3, rGO6, rGO9, and rGO12. Inset shows a digital photo of the samples and magnification of characteristic absorption peak at the rGO12 spectrum

The changes in the color of as-prepared samples are good indicator of the reduction processes of the graphene and its related material. Inset in Fig. 2 shows the yellow–brown color of the GO sample gradually darkened and change to black at the last sample, i.e., rGO12 with light supernatants indicating the degree of reduction and the graphene's hydrophobic nature have occurred successfully [64].

3.1.3 Raman spectroscopy study

Raman spectrum is an efficient tool for study the structure of graphene and its derivatives like GO and rGO [65]. Figure 3 shows the G-band, D-band, and overtone 2D-band in Raman spectra for the free-standing films of GO, rGO3, rGO6, rGO9, rGO12, and graphite powder. The G-band at 1580 cm^{-1}

represents the in-plane vibration, and D-band at 1350 cm^{-1} represents the out-plane vibration due to the defects. The intensity ratios of D and G bands (I_D/I_G) were calculated to be 0.608, 0.694, 0.700, 0.704, and 0.724 for GO, rGO3, rGO6, rGO9, and rGO12, respectively. The increase in the I_D/I_G indicates that the defects have been increased when the electrochemical reduction degrees have been increased due to the removal of oxygen-containing functional groups from GO sheets. Therefore, this removal led to a decrease in the average size of the in-plane sp2 domain, and it created defects in the basal plane of the rGOx [66–69]. On the other hand, the 2D-band shows blue-shifts from 2658 cm^{-1} of GO to 2658, 2666, 2668, 2673, and 2675 cm^{-1} of rGO3, rGO6, rGO9, and rGO12, respectively, as shown in the inset of Fig. 3. These shifts with increasing the electrochemical reduction degrees are indicative of the degrees of reduction as referred by Yang, Dongxing, et al. [70]. Also, the more shifting value is between GO and rGO3 and gradually decreases between others, confirming that the large oxygen-containing functional groups have been removed in the beginning electrochemical reduction cycles. Finally, the small and broad peak of the 2D-band in all spectra indicates that the free stand films have multi-layers of graphene [71].

Fig. 3

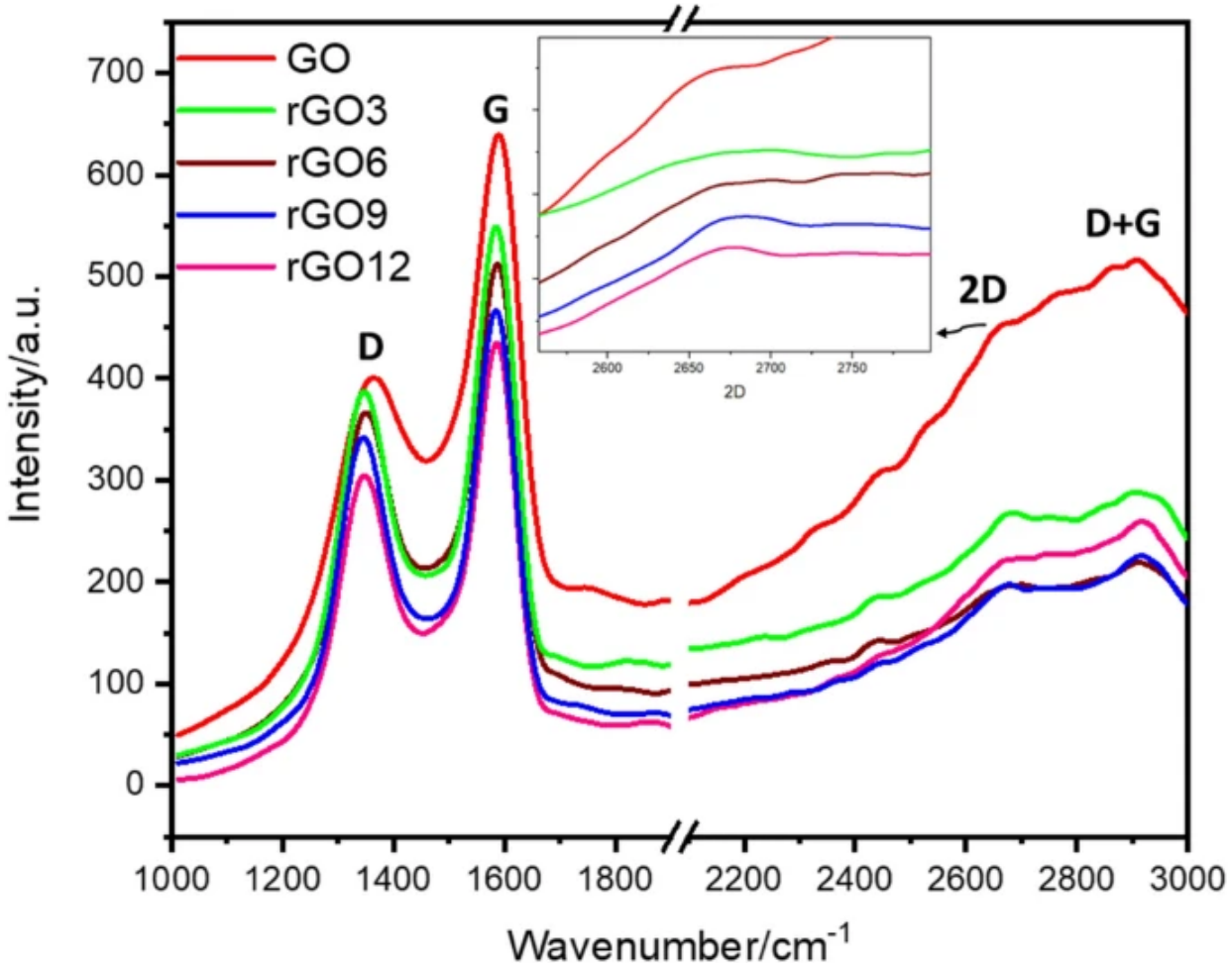

Raman spectra of GO, rGO3, rGO6, rGO9, and rGO12. Inset shows the 2D band of the GO, rGO3, rGO6,

rGO9, and rGO12

3.2 Structural and morphological characterizations

3.2.1 XRD study

The raw material (i.e., graphite) and prepared free stand films of GO, rGO3, rGO6, rGO9, and rGO12 were structurally characterized by Powder-XRD (from down to up), respectively, as shown in Fig. 4. The XRD patterns of graphite powder showed its inherent diffraction peak at 26.6° indexed to (002) crystal plane with a d-spacing of 0.33 nm. This diffraction peak totally shifted to 10.8° with an extension of d-spacing until 0.82 nm after the oxidation process due to the inserting of oxygen-containing functional groups between graphite sheets by the aid of oxidant media, as shown in the GO diffraction pattern in Fig. 4a. However, the diffraction patterns of electrochemical reduction samples (rGO3–rGO12) showed gradually decreasing in the GO diffraction peak respectively; meanwhile, a new broad diffraction peak at 24.8° has been grown gradually with increasing of electrochemical reduction degree as shown in Fig. 4b. The d-spacing of reduction diffraction peak compressed until 0.36 nm resulting in the removal of oxygen-containing functional groups between GO sheets. The small secondary peaks present in the XRD patterns of the high degrees of reduction, i.e., rGO9 and rGO12 came from ash impurities that are usually present in graphite powder sources due to their thermal treatment when manufactured, as shown in (supplementary information) Figure S1.3. Moreover, these peaks have disappeared from the XRD patterns of GO, rGO3, and rGO6 due to the incorporation and encapsulation of the graphite sheets with the oxygen-containing functional groups. These results are coincident with ATR-IR results confirming that the electrochemical reduction degrees were successfully achieved [31, 54, 63, 65–67].

Fig. 4

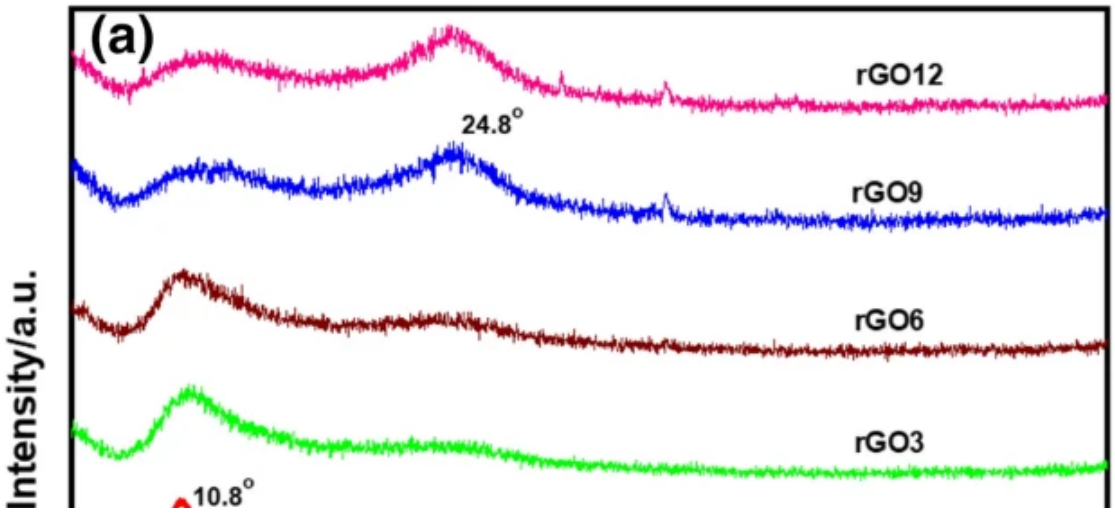

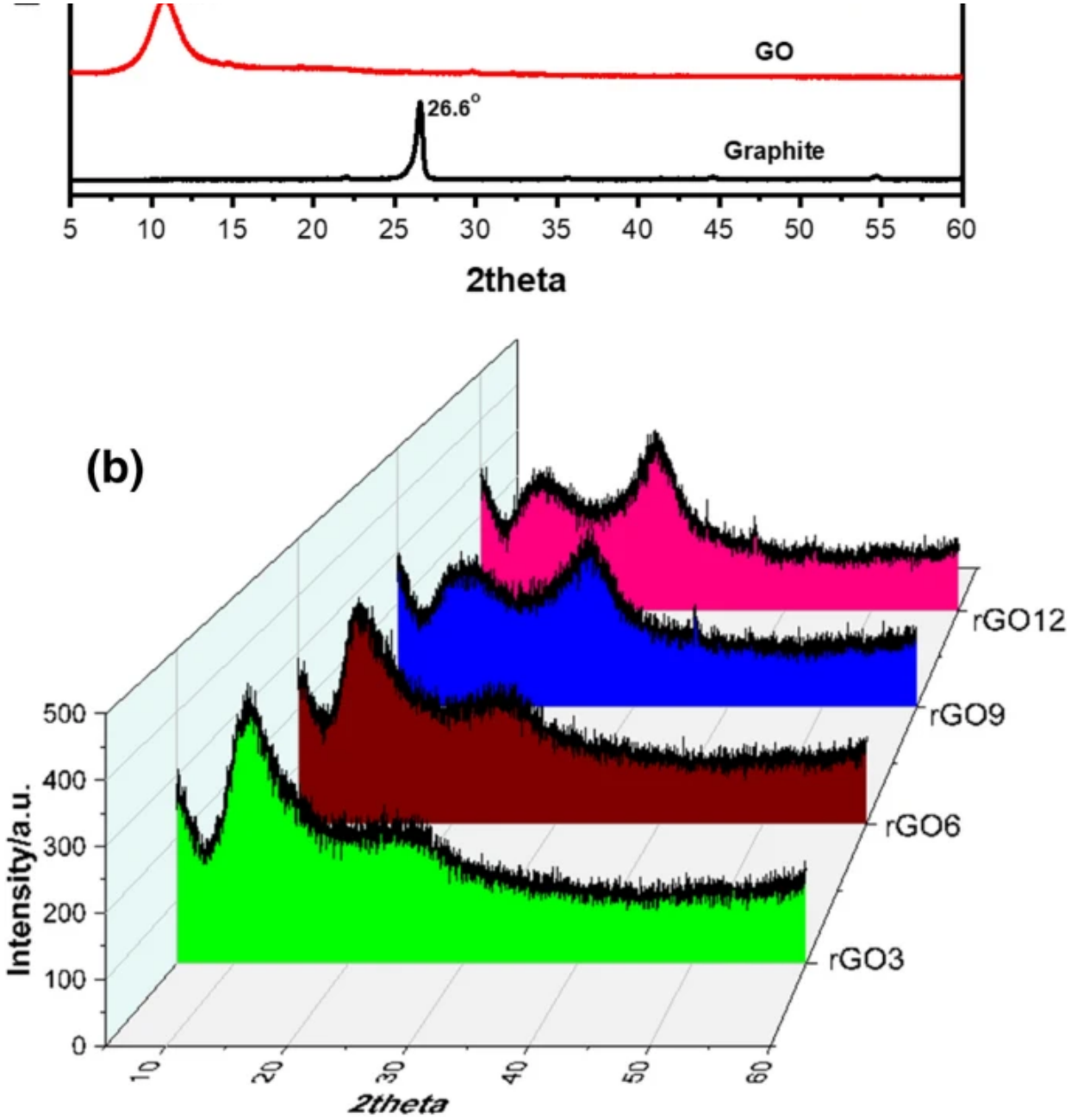

Powder-XRD patterns of **a** Graphite, GO, rGO3, rGO6, rGO9, and rGO12 (from down to up), respectively, and **b** 3-D comparison graphs of rGO3, rGO6, rGO9, and rGO12 (from front to back) respectively

3.2.2 FESEM, EDX, and AFM study

Figure 5 shows the FESEM images with EDX of GO and rGO12 powder samples at two scales (i.e., 1 µm and 500 nm). As shown in Fig. 5a and b, the large size and aggregation sheet of GO has been observed without noticeable edges in the 1 µm scale. This indicates the large size of GO sheets over 1 micron which confirms the purpose of using expanded graphite (EG). However, these sheets on the same scale have largely defected and average size decreases after electrochemical reduction due to the removal of

the oxygen-containing functional groups from the basal plane and edges of rGO12 as shown in Fig. 5c and d. These results are in agreement with Raman investigations. The EDX was done simultaneously with the FESEM measurements to compare the amount of carbon to oxygen ratio (C/O) before and after the electrochemical reduction process. As shown in Fig. 5e and f, the C/O are 1.998 and 5.488 for GO and rGO12, respectively. The results indicate the removal of oxygen molecules from the oxygen-containing functional groups existing on the rGO sheets. For further morphological investigations, the AFM images were taken. Figure 6 shows the AFM images of bare ITO, GO/ITO, and rGO12/ITO. The bare ITO topography shows the sharpest roughness and irregular surface, as shown in Fig. 6a. However, after the GO was deposited on the bare ITO by spin coating, it appeared a uniform surface topography, indicating that the GO sheets covered the sharpest roughness of the bare ITO surface, as shown in Fig. 6b and d. Moreover, the little increases in the roughness height indicate that a few GO sheets were deposited on the bare ITO. After electrochemical reduction, the rGO 12/ITO showed more uniform surface topography and relatively less roughness due to removing the oxygen-containing functional groups, as shown in Fig. 6c and e.

Fig. 5

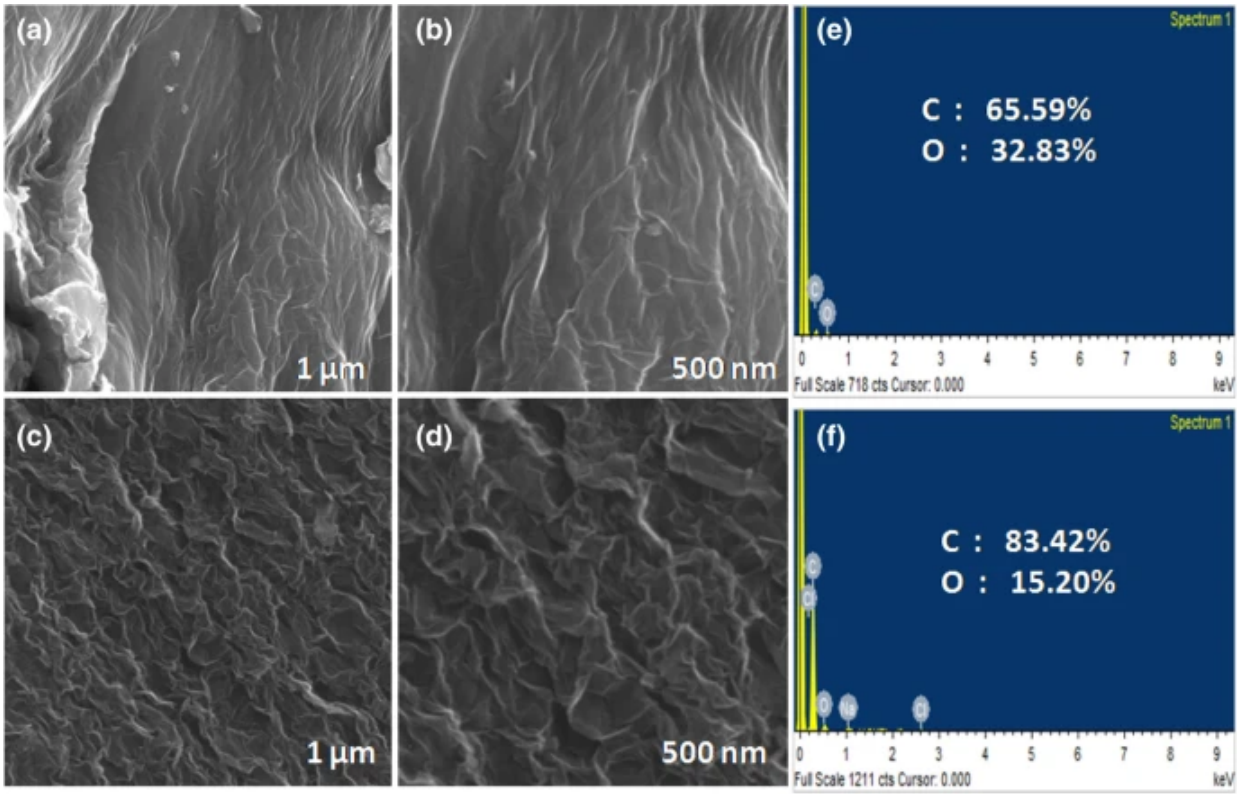

FESEM images of **a** and **b** GO on the scale of 1 µm and 500 nm, respectively, and **c** and **d** rGO12 on 1 µm and 500 nm, respectively, and EDX spectra of **e** GO and **f** rGO12

Fig. 6

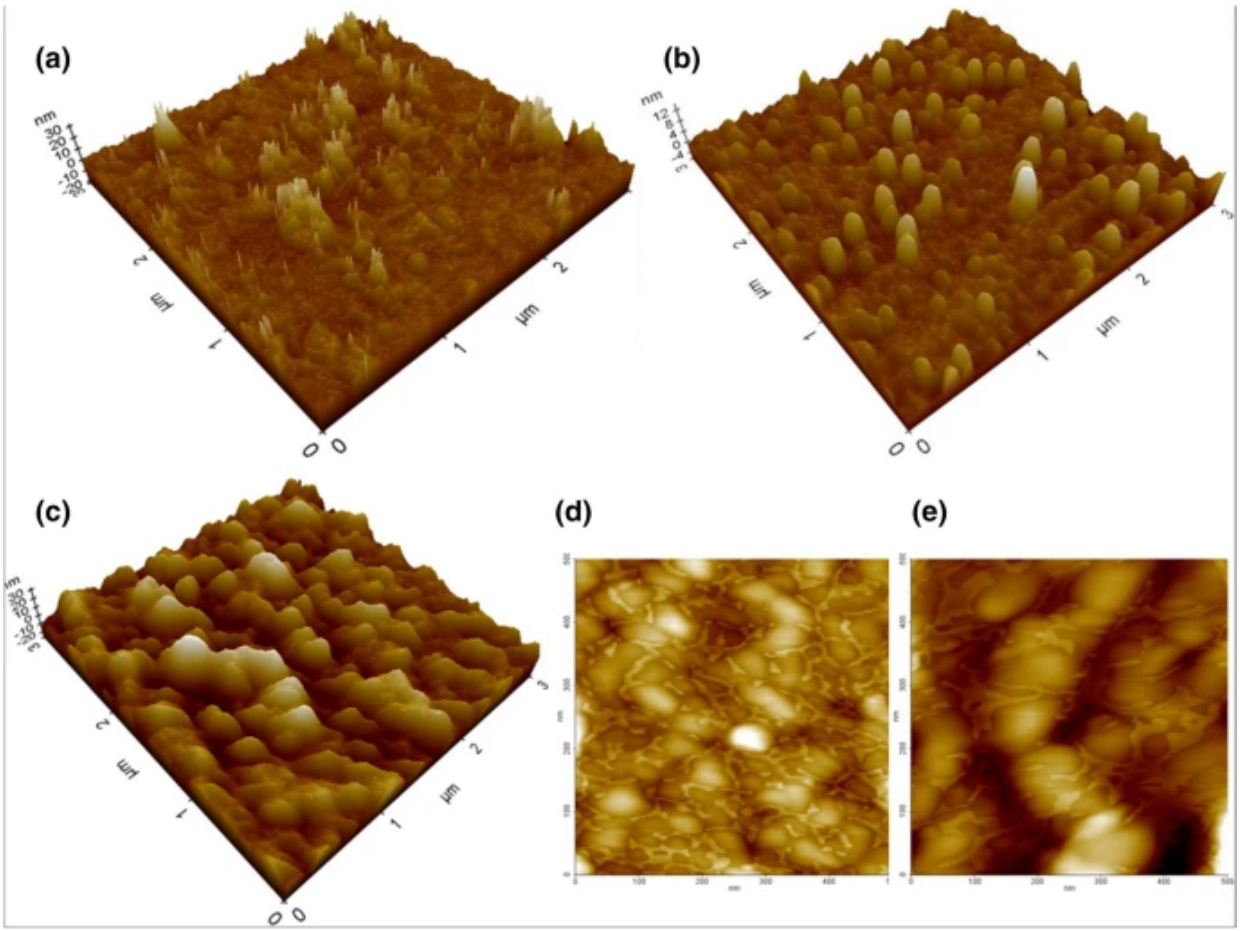

Non-contact AFM images of **a** bare ITO, **b** GO/ITO and **c** rGO12 on the scale of 5 μm, and **d** GO and **e** rGO12 on 500 nm. All the samples were spin-coated on ITO substrates

3.3 Electrochemical characterizations of reduction degree of rGO-based electrodes

3.3.1 Electrochemical reduction behavior of the GO-based electrodes.

Before studying the electrochemical reduction behavior of rGO in a supporting electrolyte, It should be noted that the exact way of this approach is not entirely known. Therefore, it still needs further investigation. However, electron exchange between the working electrode and GO in the presence of hydrogen ions produced from the electrolyte (i.e., protonation processes) plays an essential role in the electro-reduction process [65, 66]. This reaction may be described by Scheme 1.

Scheme 1

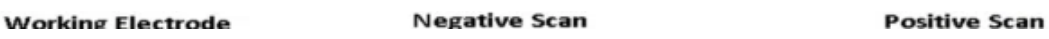

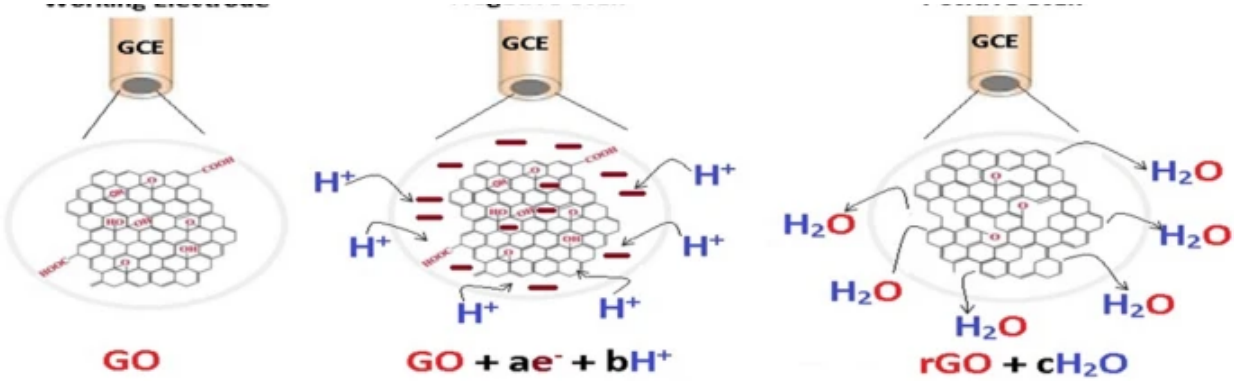

Schematic diagram of the electrochemical reduction mechanism of graphene oxide by CV technique

Figure 7 shows the cyclic voltammograms (CVs) of electrochemical reduction processes for rGO3, rGO6, rGO9, and rGO12 which exhibit approximately identical CVs except for the number of voltammetric cycles. Furthermore, the CVs show that the larger reduction part of oxygen-containing functional groups has been removed in the first voltammetric cycle with sharp and broad reduction peaks at − 1.1 and − 1.5 V, respectively. The sharp reduction peak represents the reduction of the weak oxygen-containing functional groups located on the basal plane of GO sheets within non-covalent interaction. However, the broader reduction peak at − 1.5 V attributes to the reduction of the strong oxygen-containing functional groups located at the edges and defects of the GO sheets. The rest of the voltammetric cycles have no sharp reduction peak, just remaining the broader reduction peak at higher potential, indicating that the weak oxygen-containing functional groups located on the basal plane which have mostly been removed in the first voltammetric cycle, and the strong oxygen-containing functional groups have been gradually removed from the edges and defects of the GO sheets [68, 69].

Fig. 7

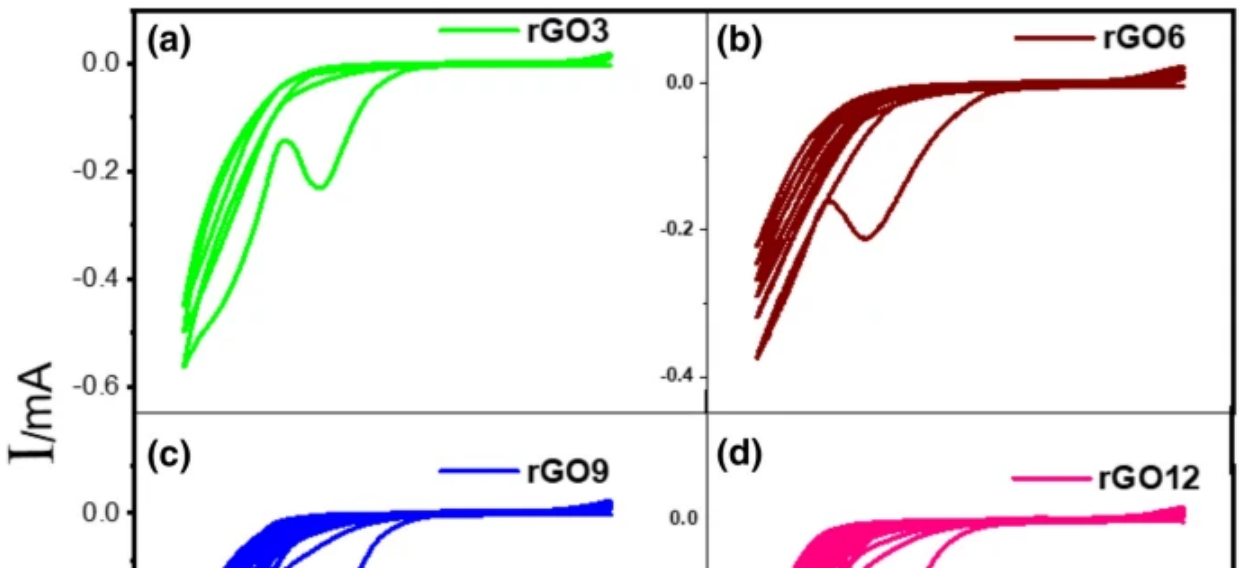

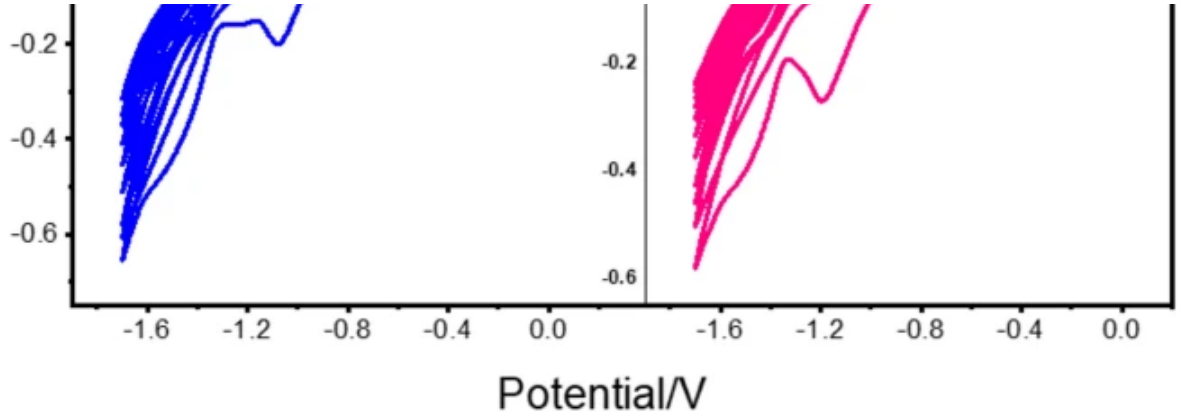

The CVs for the electrochemical reduction GCE modified with rGO3, rGO6, rGO9, and rGO12; in 0.1 M acetate buffer solution, pH 4.5; saturated with nitrogen gas. The range is between 0 and − 1.7 V and 0.05 Vs^{-1} scan rate

3.3.2 The charge-transfer behavior of modified electrodes.

The charge-transfer rate behavior at the electrode/solution interface can be explained by knowing the values of redox peak currents (I_p) and the potential difference between them (ΔE_p), and charge-transfer resistance (R_{ct}), using CV and EIS, respectively [31, 70]. Figure 8 shows the charge transfer rate features of bare and modified GCEs with GO, rGO3, rGO6, rGO9, and rGO12 which were evaluated by CV and EIS in the electrolyte (i.e., 5 mM $K_3Fe(CN)_6$ in 0.1 M KCl solution) as the electrochemical probe at the electrode/solution interface [31]. The detailed measurements of Fig. 8 are presented in Table 1. Figure 8a shows all the recorded CVs which could be seen that the $[Fe(CN)_6]^{3-/4-}$ redox reaction at the bare GCE is a quasi-reversible redox process with ΔE_p = 82 mV. Also, the anodic and cathodic peak currents have a ratio of about 1:1 representing that the GCE has manifested a well-behaved reaction interface to the $[Fe(CN)_6]^{3-/4-}$ couple [55]. However, for the GO modified GCE (GO/GCE), both redox peak currents were relatively increased due to the interaction between electrolyte species in the solution and oxygen-containing functional groups existed on the GO sheets based electrode. Moreover, the value of ΔE_p = 149 mV was increased due to the electron transfer inhibition due to the GO's low conductivity nature. Nevertheless, the degrees of electrochemical reduction increase, the ΔE_p gradually decreases with values of 94, 91, 90, and 88 mV for GCEs modified with the rGO3, rGO6, rGO9, and rGO12, indicating that the enhancement of charge-transfer rate was due to the removal of the oxygen-containing functional groups from GO sheets during the electrochemical reduction processes. However, the CVs showed a gradual increase of I_p at the rGO3 and rGO6, and then decrease at rGO9 and rGO12. The increase indicates the removal of the weak oxygen-containing functional groups and the decrease indicates that the relatively strong oxygen-containing functional groups have been removed depending on their type and location. Moreover, the relative change of I_p at the higher reduction degree is small compared with the lower reduction degree which confirms that a

large amount of weak oxygen-containing functional groups was removed in the beginning of voltammetric cycles.

Fig. 8

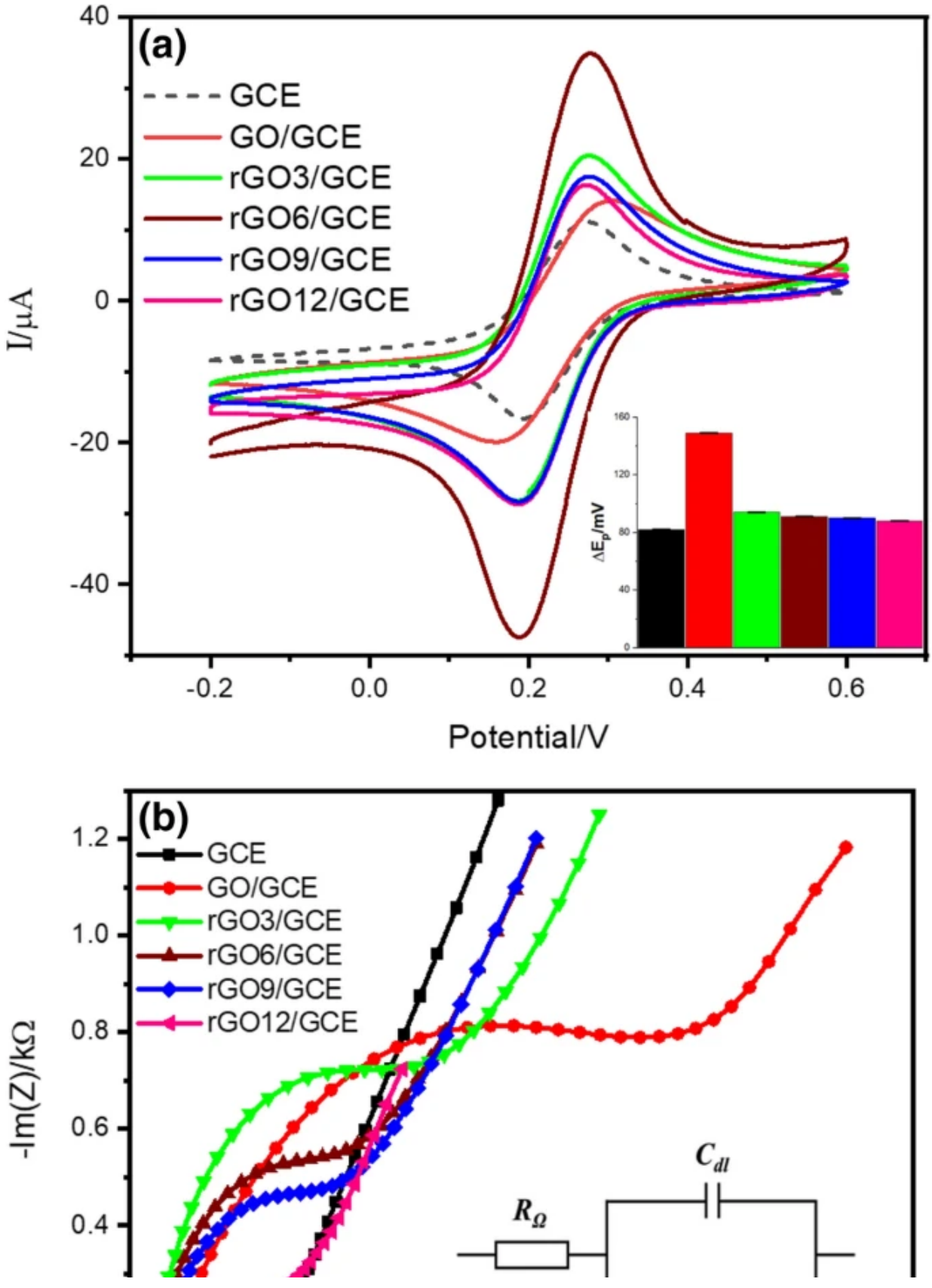

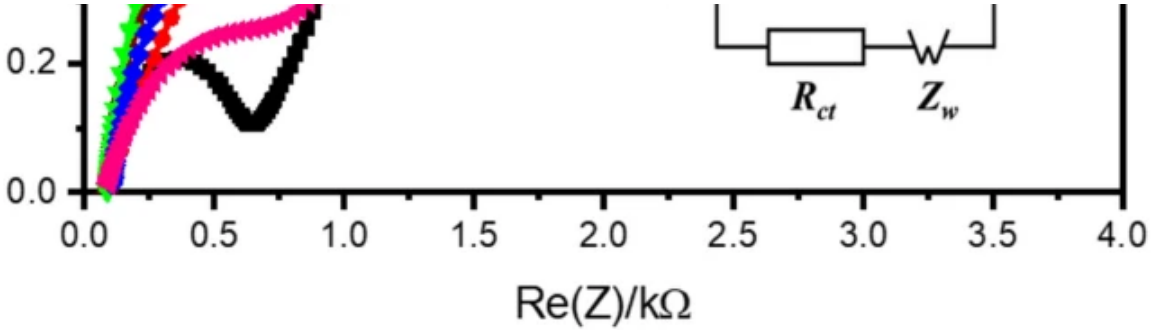

The behavior of charge-transfer rate is evaluated by using: **a** CV and **b** EIS techniques for bare GCE, GO/GCE, rGO3/GCE, rGO6/GCE, rGO9/GCE, and rGO12/GCE; in 0.1 M KCl solution containing 5 mM $K_3Fe(CN)_6$ as a redox probe system. The scan rate is 0.5 Vs^{-1} repeated in the range between - 0.2 and 0.6 V, the frequency range is between 0.1 and 10^5 Hz while applying the 0.2 V AC amplitude. The insets in Fig. 8 **a** and **b** demonstrate histogram plot including error bare of ΔE_p and the fitting electrical circuit for the EIS data, respectively

Table 1 CV and EIS parameters of bare and modified GCE

Therefore, the rGO6/GCE shows desired oxygen-containing functional groups which can work as the efficient chelating ligands for HMIs sensing applications.

EIS was used to monitor the electron transfer between the electroactive species in a solution and the underlying electrode [71, 72]. Figure 8b shows the EIS Nyquist plots for bare and modified GCEs with the GO, rGO3, rGO6, rGO9, and rGO12 at AC 0.2 V amplitude within the frequency range between 0.1 and 10^5 Hz. According to the plots, there are semi-circles and a straight line at high and low-frequency regions, respectively. For fitting EIS data, the Randles circuit model, $R_s + C_{dl}/(R_{ct} + Z_W)$, was used; where R_s is the electrolyte resistance, C_{dl} is double-layer capacitance, R_{ct} is charge-transfer resistance, and Z_W is Warburg impedance. The diameter of the semicircle represents the charge-transfer resistance R_{ct} at the electrode/electrolyte interface. The R_{ct} values were calculated to be 527, 3002, 1347, 987, 925, and 754 Ω for unmodified GCE and modified GCEs by GO, rGO3, rGO6, rGO9, and rGO12, respectively. These results exhibited agreement with that of the CV characterizations in terms of charge transfer rate.

3.4 Stripping behavior for HMIs

3.4.1 The anodic stripping voltammetric responses for HMIs at the modified GCEs.

The sensor specifications for the as-prepared electrodes to select the best performance electrode that can be used for further sensing study. Under arbitrary experimental conditions like deposition potential as a − 1 V, pH = 4, and 5 min accumulation time, the electrochemical measurements were carried out. The differential pulse anodic stripping voltammetry (DPASV) technique was employed for these analyses. With the supporting electrolyte containing 50 μgL^{-1} of Cd^{2+} and Pb^{2+} in the presence of 500 μgL^{-1} Bi^{3+}, the DPASV measurements were recorded at the GCEs modified with GO, rGO3, rGO6, rGO9, and rGO12, respectively, as shown in (supplementary information) Figure S2 and Fig. 9. The detailed results of Figure S2 and Fig. 9, like relative standard deviations (RSDs), response peak height, and oxidized potential status, have been illustrated in Table 2. The RSDs of six times repeated reading at GO/GCE are 24.30 and 17.80% for Cd^{2+} and Pb^{2+}, respectively, indicating bad repeatability due to the removal of weak oxygen-containing functional groups from the GO sheets during the sweeping of the stripping potential as shown in Figure S2a. Also, there is no well-defined oxidized potential and slow growth of Bi film due to the same reason. However, Figure S2b shows an optimization in the repeatability at rGO3/GCE where RSDs are 0.78 and 3.16% for Cd^{2+} and Pb^{2+} respectively, and well-defined oxidized potential due to the removal of the weak oxygen moiety from GO sheets after electrochemical reduction by three voltammetric cycles. Nevertheless, the slow growth of Bi film is still observed because the degree of reduction was not sufficient to remove all the weak oxygen-containing functional groups from the GO sheets. Figure S2c represents well-defined oxidized potential, and fast growth of Bi film deposition at rGO6/GCE after electrochemical reduction by six voltammetric cycles; the RSDs are 6.42 and 10.33% for Cd^{2+} and Pb^{2+}, respectively. However, the increase in the RSDs may be due to the highly response to the experimental conditions owing to its electrochemical conductivity improvement. After electrochemical reduction by nine voltammetric cycles, Figure S2d shows RSDs as 9.22 and 11.10% at the rGO9/GCE for Cd^{2+} and Pb^{2+}, respectively. The increase in the RSDs was due to the same reason aforementioned at the rGO6/GCE but there is a new unwanted broad peak current at the potential position between that for Cd^{2+} and Pb^{2+}, indicating the overlapping between the residuals of Cd^{2+} and Pb^{2+}. This overlap can be explained concerning the Bi film and the oxygen-containing functional groups. The latter act as nuclei for the Bi on the rGO sheets; thereby, the lack of oxygen-containing functional groups led to the loose fused alloy [73]. Again the unwanted peak increased at the rGO12/GCE due to the same reason at the rGO9/GCE as shown in Figure S2e. All the stripping peak heights for Cd^{2+} and Pb^{2+} at modified GCEs represent in Fig. 9. These results summarized in Table 2 exhibit the highest response signals for Cd^{2+} and Pb^{2+} at rGO6/GCE.

Fig. 9

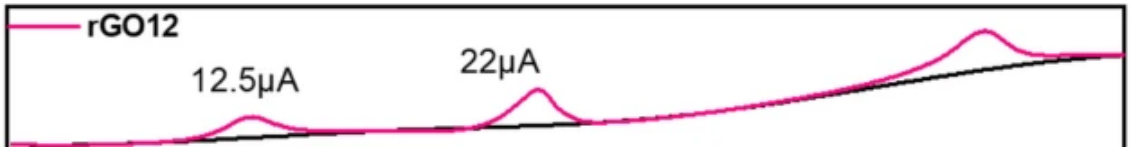

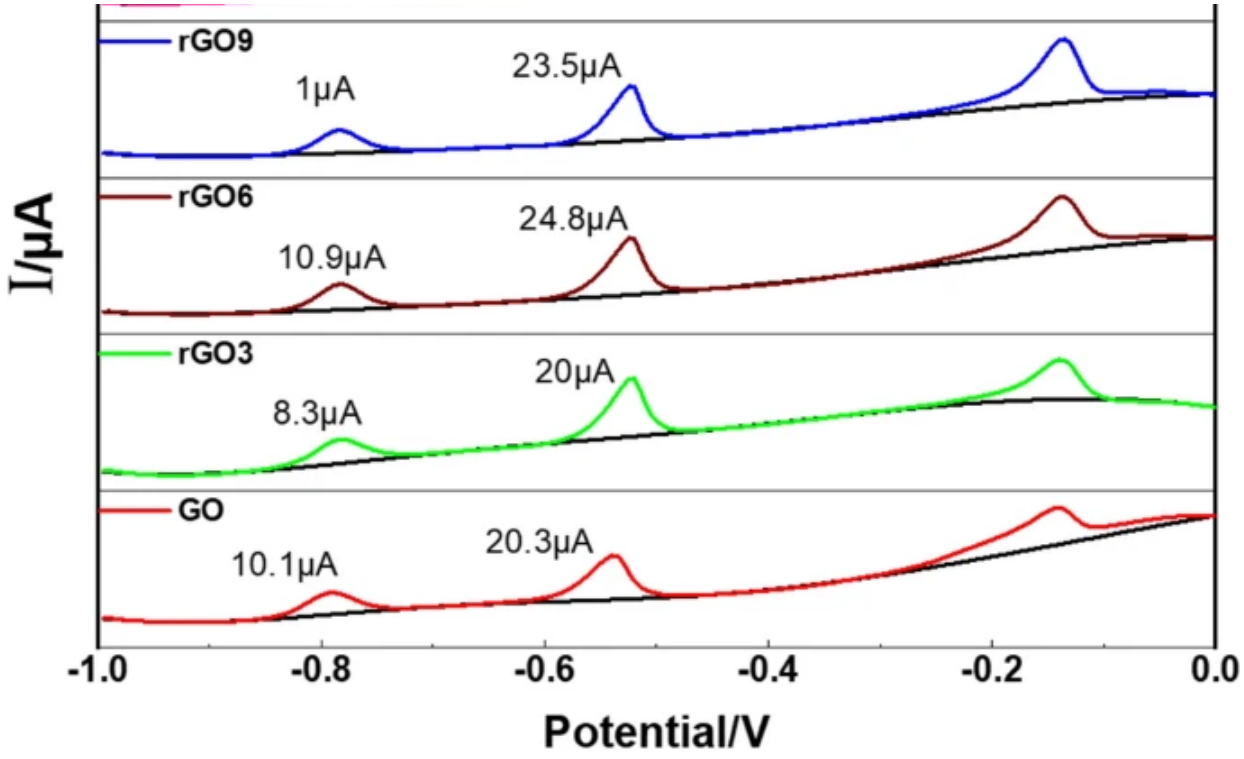

modified by GO, rGO3, rGO6, rGO9, and rGO12 in 0.1 M HAc–NaAc buffer solution which saturated with nitrogen gas, containing 50 μgL^{-1} of Cd^{2+} and Pb^{2+} in the presence of 500 μgL^{-1} Bi^{3+}

The compared staked graphs of the DPASVs for GCEs are

Table 2 the detailed comparison of the DPASV responses for HMIs at different modified GCEs

These results show that the rGO6/GCE has the highest response signals toward HMIs, well-defined oxidized potentials, and fast growth of Bi film which are entirely in agreement with that for charge-transfer analyses referred to in Sect. 3. Indeed, its repeatability was not relatively excellent, but this obstacle can be solved by optimizing the experimental conditions.

3.4.2 Electrochemical performance of modified electrodes toward HMIs.

The improvement of stripping signal responses toward Cd^{2+} and Pb^{2+} at the bare GCE and rGO6/GCE with free and presence of Bi films (i.e., Bi/rGO6/GCE and Bi/GCE) in the acetate buffer solution containing 20 μgL^{-1} of Cd^{2+} and Pb^{2+} by DPASV technique under optimal conditions were examined, as shown in Fig. 10. It can be easily seen that the voltammogram of Bi/rGO6/GCE (wine color) exhibits

anodic peak current of Cd^{2+} and Pb^{2+} higher than others by multiple folds with well-defined peak shapes centered at − 0.78 and − 0.535 V, respectively. The voltammogram of bare GCE free Bi film (Red color) does not show any appreciable stripping signal response except for Pb^{2+} due to the active graphite sites in the GCE structure. However, the stripping signals at rGO6/GCE free Bi film (Black color) show a relatively little optimization compared with those at bare GCE due to the role of the rGO as a good conducting material as well as the wealthy oxygen-containing functional groups existing on its surface led to catch HMIs. Also, they do not show well-defined oxidized potentials and bad fusing of the stripping signals toward HMIs. Finally, the stripping voltammogram of bare Bi/GCE in the presence of Bi^{3+} (Green color) shows good stripping signals response with well-defined oxidized potentials due to the role of Bi film which improves the fusing of HMIs and less susceptible to oxygen background interference [14, 74].

Fig. 10

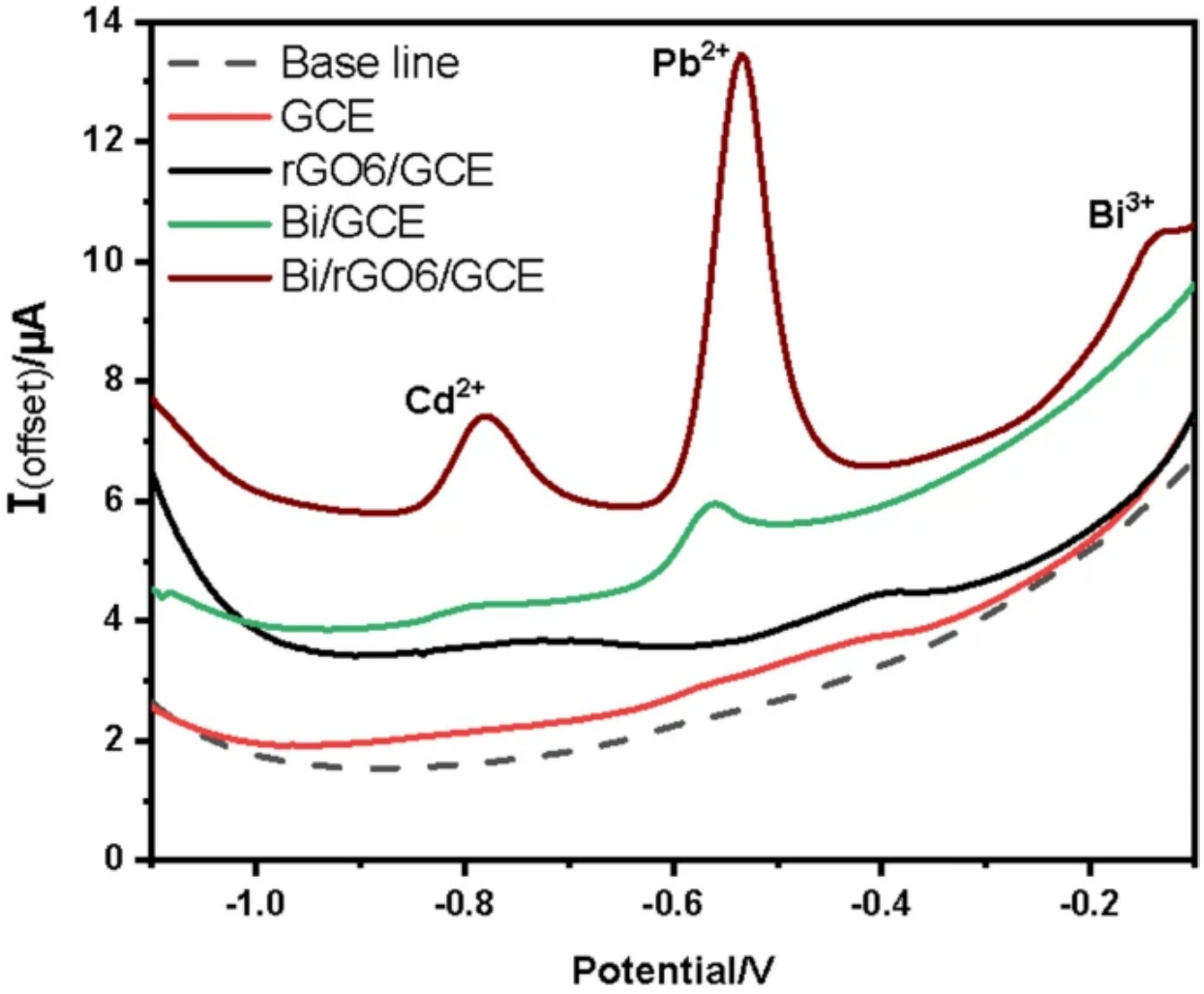

DPASVs of: bare-GCE, rGO6/GCE, Bi/GCE, Bi/rGO6/GCE in 0.1 M HAc-NaAc buffer solution; saturated with nitrogen gas, containing 20 μgL^{-1} of Cd^{2+} and Pb^{2+} and 500 μgL^{-1} Bi^{3+}. The dashed line represents the baseline of GCE in a blank buffer solution

3.4.3 Optimizations of anodic stripping voltammetry

The height and shape of anodic stripping voltammetry signals of HMIs depend on the various parameters like a supporting electrolyte, pH value, deposition potential, and accumulation time. The effect of supporting electrolyte was solved by selecting the 0.1 M acetate buffer (HAc-NaAc) solution containing 500 μgL^{-1} Bi^{3+} as a referred in many sources [75–77]. The favorable pH value was chosen after studying the effect of pH on the stripping signals toward 40 μgL^{-1} of Cd^{2+} and Pb^{2+} in the supporting electrolyte in the range between 3 and 9, as shown in Fig. 11a. The maximum stripping signals were at pH = 4.5. The decrease in the stripping signal at the pH value lower and higher than 4.5 can be assigned to the protonation with the oxygen-containing functional groups on the surface of rGO

and hydrolysis of the HMIs in the supporting electrolyte, respectively. Thus, pH = 4.5 was selected as the optimal pH for further analysis. It is essential to select an appropriate deposition potential to obtain the highest sensitivity. The Fig. 11b shows the study of the effect of deposition potential on the stripping signals toward 40 μgL^{-1} of Cd^{2+} and Pb^{2+} in supporting electrolyte in the range between − 6 and − 1.6 V. In this Figure; the inset shows two dot lines (red and black colors) for Cd^{2+} and Pb^{2+}, respectively. The increase in the deposition potential led to an increase in the amount of HMI species on the electrode surface due to the electrostatic interaction. Here, the deposition potential was selected as − 1.4 V where the Cd^{2+} and Pb^{2+} get saturated without remaining residuals of the HMIs after the stripping step. The increasing of the deposition potential behind − 1.4 V showed an appreciable increase in the stripping signal of Pb^{2+}, but this was not considered due to the remaining residuals of the HMIs after the stripping step (poor preconditioning). In this case, the poor preconditioning of the underlined electrode at the higher negativity deposition potential was due to the formation of H^+ from reducing the water that will reduce the efficiency of electrode recovering [78]. The effect of accumulation time on the stripping signals was demonstrated in Fig. 11c. The inset in Fig. 11c represents the relationship of the accumulation time and stripping current peaks toward 40 μgL^{-1} of Cd^{2+} and Pb^{2+} in the range between 30 and 300 s in the supporting electrolyte. The stripping signals clearly show direct proportional with the accumulation time. However, the stripping signals after 240 s have a low slope, indicating the lowering in the response of stripping signals with increasing the accumulation time.

Fig. 11

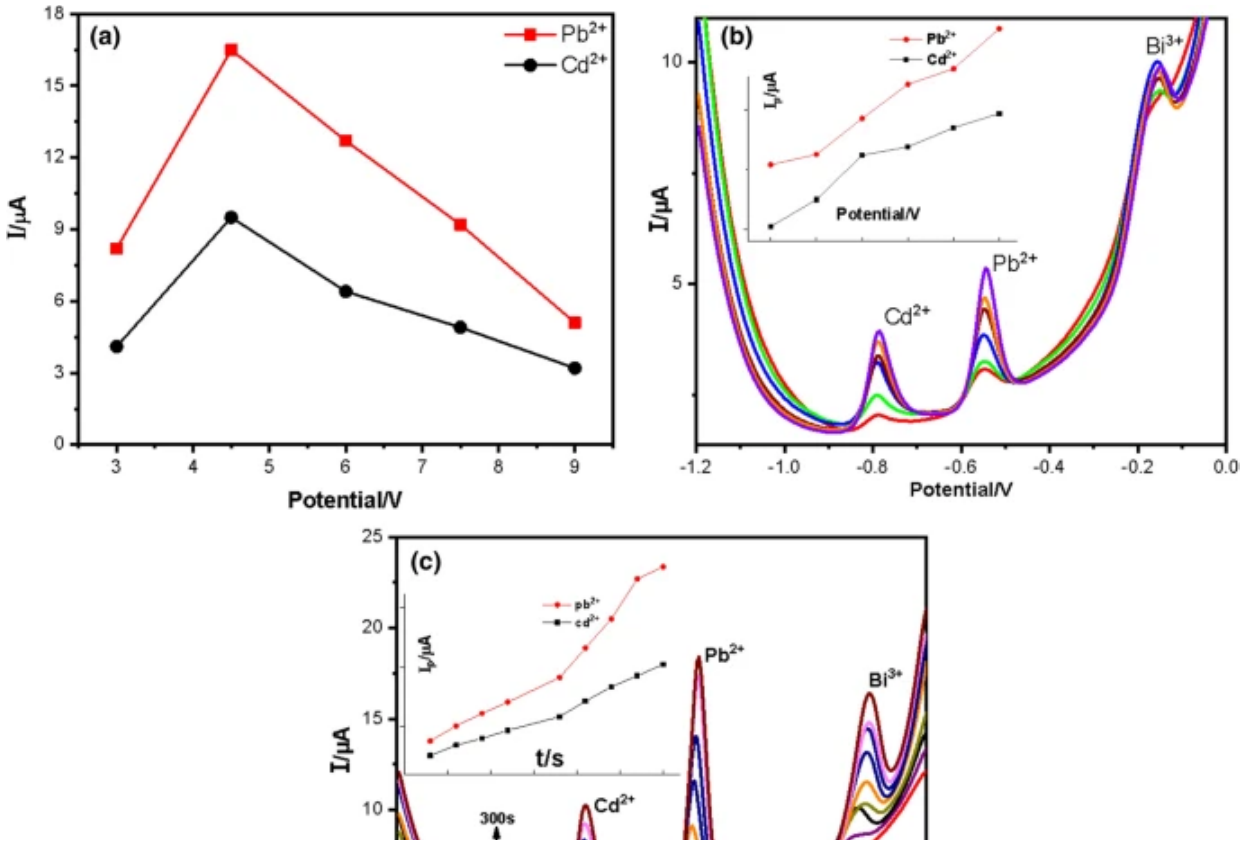

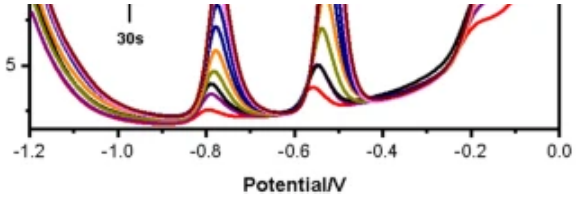

DPASVs show the effect of **a** pH, **b** deposition potential and **c** accumulation time on the stripping peak currents of Cd^{2+} and Pb^{2+} from the Bi/rGO6/GCE in 0.1 M HAc-NaAc buffer solution containing 40 μgL^{-1} of Cd^{2+} and Pb^{2+} and 500 μgL^{-1} Bi^{3+} saturated with nitrogen gas. The Insets in Figures **b** and **c** show the linear relations between stripping peak currents of Cd^{2+} and Pb^{2+} with deposition potential and accumulation time, respectively

Therefore, the optimized conditions like the supporting electrolyte, pH value, deposition potential, and accumulation time were chosen to be 0.1 M HAc-NaAc solution containing 500 μgL^{-1} Bi^{3+}, 4.5, − 1.4 V, and 240 s, respectively.

3.4.4 Analytical features of the modified electrode

The Bi/rGO6/GCE electrode was used to perform the simultaneous detection of Cd^{2+} and Pb^{2+} under the optimized conditions. Figure 12 shows the DPASVs at varying Cd^{2+} and Pb^{2+} concentrations. The stripping peak current signals in the scale of µA were linearly proportional to the concentration of the HMIs in the range between 10 and 50 μgL^{-1} with 6 number of data points. The limit of detection (LOD) values of Cd^{2+} and Pb^{2+} were calculated to be 1.2 and 0.2 μgL^{-1} respectively, with the signal to noise ratio (S/N) equals 3. These results have been calculated by using a [LOD = 3.3 S_y/S] formula; where S_y is the standard deviation of the response at a level near the blank solution (i.e., seven times) as shown in (supplementary information) Figure S4; S is the slope of the calibration curve; detailed calculations have been represented in the supplementary information S4.1. The regression equations are: I (µA) = 0.2c (μgL^{-1}) − 0.3; (R^2 = 0.991) and I (µA) = 0.4c (μgL^{-1}) − 1; (R^2 = 0.974) for Cd^{2+} and Pb^{2+}, respectively. The calculated values of LOD for Cd^{2+} and Pb^{2+} were lower than that recommended by WHO for Cd^{2+} and Pb^{2+} (i.e., 3 and 10 μgL^{-1}, respectively) in drinking water [4].

Fig. 12

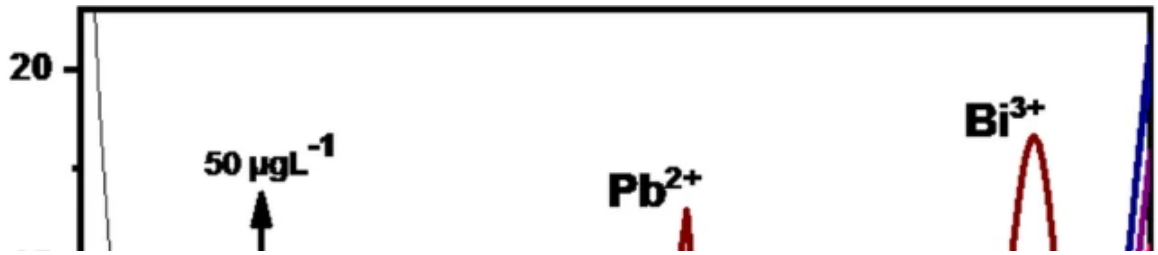

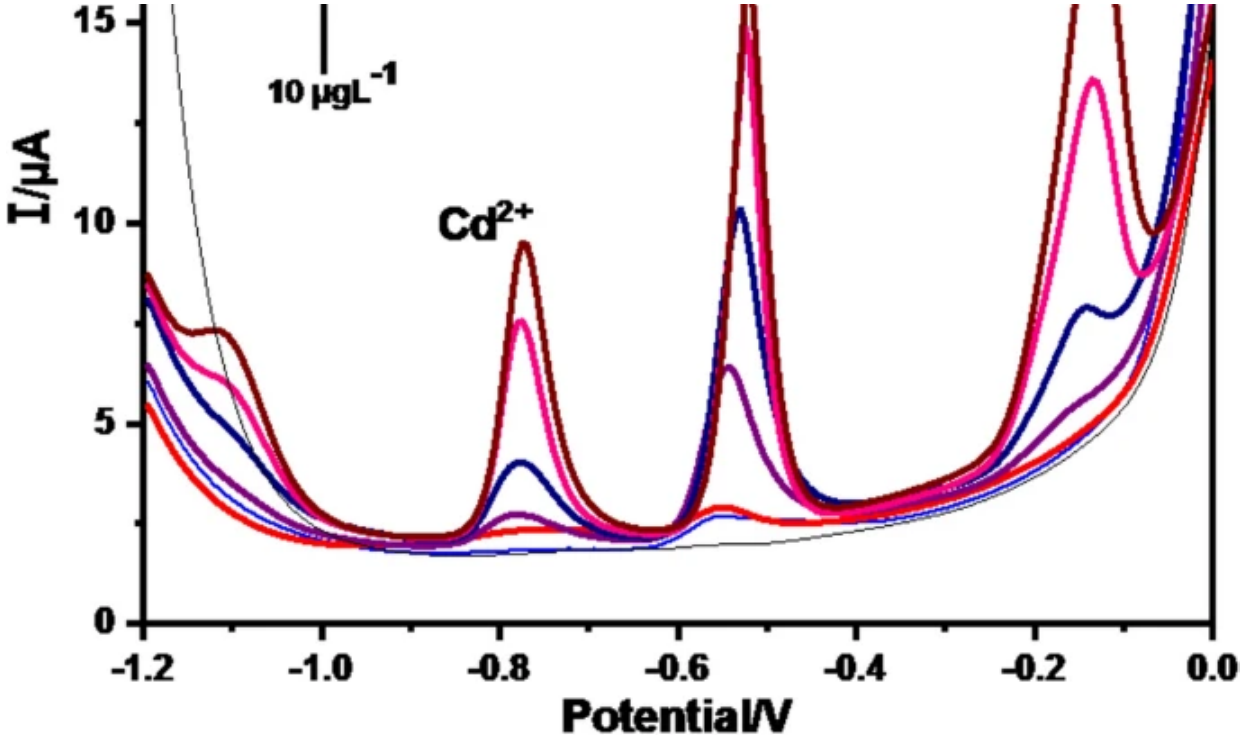

The DPASV for various concentrations (0, 10, 15, 20, 30, 40 and 50 μgL^{-1} from bottom to top) of Cd^{2+} and Pb^{2+} on the Bi/rGO6/GCE. Supporting electrolyte: 0.1 M acetate buffer (pH = 4.5) containing 500 μgL^{-1} of Bi^{3+} and other HMIs under optimal conditions

The stability of the electrochemical sensor was investigated in terms of repeatability and reproducibility by the DPASV technique under the optimized conditions. For the study of the repeatability of the electrode, seven successive measurements were carried out using the same sensor toward 15 μgL^{-1} of Cd^{2+} and Pb^{2+}. The RSDs were calculated for the Bi/rGO6/GCE to be 2.9 and 0.7% for Cd^{2+} and Pb^{2+} respectively, as shown in (supplementary information) Figure S3. The reproducibility and stability of the electrochemical sensor were investigated using four Bi/rGO6/GCEs that were prepared similarly. Weekly, one of these electrodes was used for one time for measuring the linear ranges. The obtained linear ranges and detection limits of the electrochemical responses were similar as shown in (supplementary information) Figure S3.1.

The analytical performance of this modified electrode was compared with different modified electrodes and detailed results shown in Table 3. Although this work is an inexpensive and green approach, it is clear that the Bi/rGO6/GCE shows the lower RSDs, indicating the highest stability due to selecting the best reduction degree of rGO that achieved high electrochemical sensing performance toward HMIs detection. However, the LOD shows a lower value for Pb^{2+} and acceptable value for Cd^{2+}; both are much lower than the recommended values in drinking water assigned by the WHO.

Table 3 A comparison between the analytical performances of different modified electrodes has been reported for detecting the Pb^{2+} and Cd^{2+} in aqueous media

It can be concluded here that all these studies indicated that the prepared electrochemical sensor has good sensitivity, repeatability, reproducibility, and stability.

4 Conclusion

In summary, a green and simple approach for different degrees of rGOx-based electrodes was prepared, characterized, and applied for the detection of HMIs in presence of Bi. Among different reduction degrees of rGOx-based electrodes, the Bi/rGO6/GCE exhibited excellent stability and desired response signal toward HMIs. This electrode was considered as the desired electrode for the electrochemical sensor which was then used for further electrochemical analysis. Under optimized conditions, the Bi/rGO6/GCE showed excellent electrochemical performance toward HMIs and detected Cd^{2+} and Pb^{2+} to the levels under toxic levels determined by WHO. This study aimed at understanding the relationship between the structure of reduced graphene oxide and its affinity toward HMIs. Finally, it concluded that the specific degree of the rGOx is going to play a significant role in achieving better sensitivity, stability, and LOD values toward HMIs detection.

References

1. K. Subrahmanyam et al., Simple method of preparing graphene flakes by an arc-discharge method. J. Phys. Chem. C **113**(11), 4257–4259 (2009)

Article Google Scholar

2. K.-H. Wu et al., Electrochemical detection of heavy metal pollutant using crosslinked chitosan/carbon nanotubes thin film electrodes. Mater. Express **7**(1), 15–24 (2017)

Article ADS Google Scholar

3. Y. Zhu et al., Graphene and graphene oxide: synthesis, properties, and applications. Adv. Mater. **22**(35), 3906–3924 (2010)

Article Google Scholar

4. WHO, *Guidelines for Drinking-Water Quality* (World Health Organization, Geneva, 2011), pp. 303–304

Google Scholar

5. H. Shimizu, S. Nagase, M. Ikeda, Alternating current surface photovoltage in thermally oxidized chromium-contaminated n-type silicon wafers. Appl. Phys. A **104**(3), 929–934 (2011)

Article ADS Google Scholar

6. H. Jiang, B. Hu, Determination of trace Cd and Pb in natural waters by direct single drop microextraction combined with electrothermal atomic absorption spectrometry. Microchim. Acta **161**(1–2), 101–107 (2008)

Article Google Scholar

7. R.S. Shemshadi et al., Determination of cadmium and zinc in waters by flame atomic absorption spectrometry after cloud-point extraction. J. Anal. Chem. **67**(6), 577–580 (2012)

Article Google Scholar

8. Y.-L. Feng et al., Sequential determination of tin, arsenic, bismuth and antimony in marine sediment material by inductively coupled plasma atomic emission spectrometry using a small concentric hydride generator and L-cysteine as prereductant. Fresenius' J. Anal. Chem. **361**(2), 155–157 (1998)

Article Google Scholar

9. M. Galiová et al., Investigation of heavy-metal accumulation in selected plant samples using laser induced breakdown spectroscopy and laser ablation inductively coupled plasma mass spectrometry. Appl. Phys. A **93**(4), 917–922 (2008)

Article ADS Google Scholar

10. A.M. Massadeh, A.-W.O. El-Rjoob, S.A. Gharaibeh, Analysis of selected heavy metals in tap water by inductively coupled plasma-optical emission spectrometry after pre-concentration using chelex-100 ion exchange resin. Water Air Soil Pollut. **231**(5), 243 (2020)

Article ADS Google Scholar

11. P. Suwannasom, C. Ruangviriyachai, Simultaneous quantification of Cd, Cu, Pb and Zn in Thai fermented food by DPASV with a microwave digestion. Int. Food Res. J. **18**(2), 803 (2011)

Google Scholar

12. J.A. Barón-Jaimez, J.L. Marulanda-Arévalo, J.J. Barba-Ortega, Electrodes friendly with the environment for detect heavy metal. Dyna **81**(187), 122–128 (2014)

Article Google Scholar

13. H. Xu et al., A Nafion-coated bismuth film electrode for the determination of heavy metals in vegetable using differential pulse anodic stripping voltammetry: an alternative to mercury-based electrodes. Food Chem. **109**(4), 834–839 (2008)

Article Google Scholar

14. V. Rehacek et al., Bismuth film electrodes for heavy metals determination. Microsyst. Technol. **14**(4–5), 491–498 (2008)

Article Google Scholar

15. A.P.R. de Souza et al., Screen-printed back-to-back electroanalytical sensors: heavy metal ion sensing. Analyst **140**(12), 4130–4136 (2015)

Article ADS Google Scholar

16. J. Fowler et al., Practical chemical sensors from chemically derived graphene. ACS Nano **3**, 301–306 (2009)

Article Google Scholar

17. G. Grasso et al., A mass spectrometry and surface enhanced raman spectroscopy study of the interaction between linear carbon chains and noble metals. Carbon **47**(11), 2611–2619 (2009)

Article Google Scholar

18. D. Sanchez-Rodas et al., Atomic fluorescence spectrometry: a suitable detection technique in speciation studies for arsenic, selenium, antimony and mercury. J. Anal. At. Spectrom. **25**(7), 933–946 (2010)

Article Google Scholar

19. K. Siraj, S.A. Kitte, Analysis of copper, zinc and lead using atomic absorption spectrophotometer in ground water of Jimma town of Southwestern Ethiopia. Int. J. Chem. Anal. Sci. **4**(4), 201–204 (2013)

Article Google Scholar

20. L. Zhang et al., Three-dimensional nanoporous graphene-carbon nanotube hybrid frameworks for confinement of SnS2 nanosheets: flexible and binder-free papers with highly reversible lithium storage. ACS Appl. Mater. Interfaces. **7**(50), 27823–27830 (2015)

Article Google Scholar

21. Z.-Q. Zhao et al., Selective adsorption toward toxic metal ions results in selective response: electrochemical studies on a polypyrrole/reduced graphene oxide nanocomposite. Chem. Commun. **48**(16), 2180–2182 (2012)

Article Google Scholar

22. N. Ingle et al., ChemFET sensor: nanorods of nickel-substituted metal-organic framework for detection of SO 2. Appl. Phys. A **126**(9), 1–9 (2020)

Article Google Scholar

23. N. Ingle et al., Sulfur dioxide (SO 2) detection using composite of Nickel benzene carboxylic (Ni 3 BTC 2) and OH-functionalized single walled carbon nanotubes (OH-SWNTs). Front. Mater. **7**, 93 (2020)

Article ADS Google Scholar

24. M. Mahadik et al., EDTA modified PANI/GO composite based detection of Hg (II) ions. Front. Mater. **7**, 81 (2020)

Article ADS Google Scholar

25. P.W. Sayyad et al., Sensitive and selective detection of Cu2+ and Pb2+ ions using field effect transistor (FET) based on L-cysteine anchored PEDOT: PSS/rGO composite. Chem. Phys. Lett. **761**, 138056 (2020)

Article Google Scholar

26. P.W. Sayyad et al., Chemiresistive SO 2 sensor: graphene oxide (GO) anchored poly (3, 4-ethylenedioxythiophene): poly (4styrenesulfonate)(PEDOT: PSS). Appl. Phys. A **126**(11), 1–8 (2020)

Article ADS Google Scholar

27. S.Y. Toh et al., Graphene production via electrochemical reduction of graphene oxide: synthesis and characterisation. Chem. Eng. J. **251**, 422–434 (2014)

Article Google Scholar

28. K. Chen et al., Hg (II) ion detection using thermally reduced graphene oxide decorated with functionalized gold nanoparticles. Anal. Chem. **84**(9), 4057–4062 (2012)

Article Google Scholar

29. N. Promphet et al., An electrochemical sensor based on graphene/polyaniline/polystyrene nanoporous fibers modified electrode for simultaneous determination of lead and cadmium. Sens. Actuators B Chem. **207**, 526–534 (2015)

Article Google Scholar

30. M.A. Raj, S.A. John, Fabrication of electrochemically reduced graphene oxide films on glassy carbon electrode by self-assembly method and their electrocatalytic application. J. Phys. Chem. C **117**(8), 4326–4335 (2013)

Article Google Scholar

31. L. Tang et al., Preparation, structure, and electrochemical properties of reduced graphene sheet films. Adv. Funct. Mater. **19**(17), 2782–2789 (2009)

Article Google Scholar

32. S. Felix et al., A novel CuO–N-doped graphene nanocomposite-based hybrid electrode for the electrochemical detection of glucose. Appl. Phys. A **123**(10), 620 (2017)

Article ADS Google Scholar

33. A. Panda, P.D. Pukhrambam, G. Keiser, Performance analysis of graphene-based surface plasmon resonance biosensor for blood glucose and gas detection. Appl. Phys. A **126**(3), 153 (2020)

Article ADS Google Scholar

34. I. Shtepliuk, R. Yakimova, Interaction of epitaxial graphene with heavy metals: towards novel sensing platform. Nanotechnology **30**(29), 294002 (2019)

Article ADS Google Scholar

35. M. Kumar, J.S. Chung, S.H. Hur, Graphene composites for lead ions removal from aqueous

solutions. Appl. Sci. **9**(14), 2925 (2019)

Article Google Scholar

36. Y. Zuo et al., Graphene-derived nanomaterials as recognition elements for electrochemical determination of heavy metal ions: a review. Microchim. Acta **186**(3), 171 (2019)

Article ADS Google Scholar

37. J. Xu et al., A review of functionalized carbon nanotubes and graphene for heavy metal adsorption from water: preparation, application, and mechanism. Chemosphere **195**, 351–364 (2018)

Article ADS Google Scholar

38. X. Gong et al., Graphene oxide-based electrochemical sensor: a platform for ultrasensitive detection of heavy metal ions. RSC Adv. **4**(47), 24653–24657 (2014)

Article ADS Google Scholar

39. X. Xuan, M.F. Hossain, J.Y. Park, A fully integrated and miniaturized heavy-metal-detection sensor based on micro-patterned reduced graphene oxide. Sci. Rep. **6**, 33125 (2016)

Article ADS Google Scholar

40. M.S.A. Bhuyan et al., Synthesis of graphene. Int. Nano Lett. **6**(2), 65–83 (2016)

Article MathSciNet Google Scholar

41. R.K. Singh, R. Kumar, D.P. Singh, Graphene oxide: strategies for synthesis, reduction and frontier applications. RSC Adv. **6**(69), 64993–65011 (2016)

Article ADS Google Scholar

42. C. Punckt et al., The effect of degree of reduction on the electrical properties of functionalized graphene sheets. Appl. Phys. Lett. **102**(2), 023114 (2013)

Article ADS Google Scholar

43. D.F. Báez et al., Reduced graphene oxides: influence of the reduction method on the electrocatalytic effect towards nucleic acid oxidation. Nanomaterials **7**(7), 168 (2017)

Article Google Scholar

44. C.R. Minitha et al., Impact of oxygen functional groups on reduced graphene oxide-based sensors for ammonia and toluene detection at room temperature. ACS Omega **3**(4), 4105–4112 (2018)

Article Google Scholar

45. C. Jun-Gang et al., Influence of thermal reduction temperature on the humidity sensitivity of graphene oxide. Fuller. Nanotub. Carbon Nanostruct. **23**(5), 418–423 (2015)

Article ADS Google Scholar

46. R.D. Hancock, A.E. Martell, Ligand design for selective complexation of metal ions in aqueous solution. Chem. Rev. **89**(8), 1875–1914 (1989)

Article Google Scholar

47. W. Peng et al., A review on heavy metal ions adsorption from water by graphene oxide and its composites. J. Mol. Liq. **230**, 496–504 (2017)

Article Google Scholar

48. N.I. Kovtyukhova et al., Layer-by-layer assembly of ultrathin composite films from micron-sized graphite oxide sheets and polycations. Chem. Mater. **11**(3), 771–778 (1999)

Article Google Scholar

49. D. Li et al., Processable aqueous dispersions of graphene nanosheets. Nat. Nanotechnol. **3**(2), 101 (2008)

Article ADS Google Scholar

50. S.H. Aboutalebi et al., Spontaneous formation of liquid crystals in ultralarge graphene oxide dispersions. Adv. Funct. Mater. **21**(15), 2978–2988 (2011)

Article Google Scholar

51. X. Lin et al., Fabrication of highly-aligned, conductive, and strong graphene papers using ultralarge graphene oxide sheets. ACS Nano **6**(12), 10708–10719 (2012)

Article Google Scholar

52. B.K. Ong et al., Graphenes prepared by hummers, staudenmaier and hofmann methods for analysis of TNT-based nitroaromatic explosives in seawater. Electroanalysis **24**(11), 2085–2093 (2012)

Article MathSciNet Google Scholar

53. S. Zhou et al., Electrochemical sensing toward trace As (III) based on mesoporous MnFe2O4/Au hybrid nanospheres modified glass carbon electrode. Sensors **16**(6), 935 (2016)

Article Google Scholar

54. M.B. Vázquez-Santos et al., Comparative XRD, Raman, and TEM study on graphitization of PBO-derived carbon fibers. J. Phys. Chem. C **116**(1), 257–268 (2011)

Article Google Scholar

55. H.-L. Guo et al., A green approach to the synthesis of graphene nanosheets. ACS Nano **3**(9), 2653–2659 (2009)

Article Google Scholar

56. G.K. Ramesha, S. Sampath, Electrochemical reduction of oriented graphene oxide films: an in situ Raman spectroelectrochemical study. J. Phys. Chem. C **113**(19), 7985–7989 (2009)

Article Google Scholar

57. J.A. Quezada-Renteria et al., Influence of protons on reduction degree and defect formation in electrochemically reduced graphene oxide. Carbon **149**, 722–732 (2019)

Article Google Scholar

58. D.R. Dreyer et al., The chemistry of graphene oxide. Chem. Soc. Rev. **39**(1), 228–240 (2010)

Article Google Scholar

59. Y. Wu et al., Electrochemical detection of guaiacol in bamboo juice based on the enhancement effect of RGO nanosheets. Anal. Methods **6**(8), 2729–2735 (2014)

Article Google Scholar

60. D.C. Marcano et al., Improved synthesis of graphene oxide. ACS Nano **4**(8), 4806–4814 (2010)

Article Google Scholar

61. J. Zhang et al., Reduction of graphene oxide via L-ascorbic acid. Chem. Commun. **46**(7), 1112–1114 (2010)

Article Google Scholar

62. C. Zhang et al., Graphene oxide-assisted dispersion of pristine multiwalled carbon nanotubes in aqueous media. J. Phys. Chem. C **114**(26), 11435–11440 (2010)

Article Google Scholar

63. Huh, S.H. (2011) Thermal reduction of graphene oxide, physics and applications of graphene - experiments, Sergey Mikhailov, IntechOpen. https://doi.org/10.5772/14156. Available from: https://www.intechopen.com/books/physics-and-applications-of-graphene-experiments/

thermalreduction-of-graphene-oxide.

64. D. Chen, L. Li, L. Guo, An environment-friendly preparation of reduced graphene oxide nanosheets via amino acid. Nanotechnology **22**(32), 325601 (2011)

Article ADS Google Scholar

65. H.-W. Kim, Y.-I. Kim, Characteristics of indium-tin-oxide nanoparticles prepared by controlled chemical coprecipitation method. Bull. Korean Chem. Soc. **29**(9), 1827–1830 (2008)

Article Google Scholar

66. M.J. McAllister et al., Single sheet functionalized graphene by oxidation and thermal expansion of graphite. Chem. Mater. **19**(18), 4396–4404 (2007)

Article Google Scholar

67. Joseph T, N Thomas (2020) A facile electrochemical sensor based on titanium oxide (TiO2)/ reduced graphene oxide (RGO) nano composite modified carbon paste electrode for sensitive detection of epinephrine (EP) from ternary mixture, Materials Today: Proceedings, 2020. https://doi.org/10.1016/j.matpr.2020.05.257. Available from: http://www.sciencedirect.com/science/article/pii/S2214785320338189.

68. B. Gupta et al., Role of oxygen functional groups in reduced graphene oxide for lubrication. Sci. Rep. **7**, 45030 (2017)

Article ADS Google Scholar

69. A. Bellunato et al., Chemistry at the edge of graphene. ChemPhysChem **17**(6), 785–801 (2016)

Article Google Scholar

70. A. Ramanavicius, P. Genys, A. Ramanaviciene, Electrochemical impedance spectroscopy based evaluation of 1, 10-phenanthroline-5, 6-dione and glucose oxidase modified graphite electrode. Electrochim. Acta **146**, 659–665 (2014)

Article Google Scholar

71. W. Chen et al., High-performance nanostructured supercapacitors on a sponge. Nano Lett. **11**(12), 5165–5172 (2011)

Article ADS Google Scholar

72. Y. Sun et al., Controlled synthesis various shapes Fe3O4 decorated reduced graphene oxide applied in the electrochemical detection. J. Alloy. Compd. **638**, 182–187 (2015)

Article Google Scholar

73. G. Zhao et al., Bismuth subcarbonate decorated reduced graphene oxide nanocomposite for the sensitive stripping voltammetry analysis of Pb (II) and Cd (II) in water. Sensors **20**(21), 6085 (2020)

Article Google Scholar

74. Z. Wang, L. Li, E. Liu, Graphene ultrathin film electrodes modified with bismuth nanoparticles and polyaniline porous layers for detection of lead and cadmium ions in acetate buffer solutions. Thin Solid Films **544**, 362–367 (2013)

Article ADS Google Scholar

75. H. Huang et al., Ultrasensitive and simultaneous detection of heavy metal ions based on three-dimensional graphene-carbon nanotubes hybrid electrode materials. Anal. Chim. Acta **852**, 45–54 (2014)

Article Google Scholar

76. S. Ding et al., An electrochemical sensor of poly (edot-pyridine-edot)/graphitic carbon nitride composite for simultaneous detection of cd2+ and pb2+. Materials **11**(5), 702 (2018)

Article ADS Google Scholar

77. L. Yu et al., An electrochemical sensor based on Co 3 O 4 nanosheets for lead ions determination. RSC Adv. **7**(63), 39611–39616 (2017)

Article ADS Google Scholar

78. W. Kang et al., Determination of lead with a copper-based electrochemical sensor. Anal. Chem. **89**(6), 3345–3352 (2017)

Article Google Scholar

79. X. Xuan, J.Y. Park, A miniaturized and flexible cadmium and lead ion detection sensor based on micro-patterned reduced graphene oxide/carbon nanotube/bismuth composite electrodes. Sens. Actuators B Chem. **255**, 1220–1227 (2018)

Article Google Scholar

80. J. Ping et al., Development of an electrochemically reduced graphene oxide modified disposable bismuth film electrode and its application for stripping analysis of heavy metals in milk. Food Chem. **151**, 65–71 (2014)

Article Google Scholar

81. X. Hou et al., Determination of trace lead and cadmium in decorative material using disposable screen-printed electrode electrically modified with reduced graphene oxide/L-Cysteine/Bi-Film. Sensors **20**(5), 1322 (2020)

Article Google Scholar

82. A.C. Lazanas et al., 2D bismuthene/graphene modified electrodes for the ultra-sensitive stripping voltammetric determination of lead and cadmium. Electrochim. Acta **336**, 135726 (2020)

Article Google Scholar

Acknowledgments

The authors extend their sincere thanks to UGC—DAE CSR (RRCAT), Indore (Project No. CSR-IC-BL66/CRS- 183/2016-17/847), Inter University Accelerator Center (IUAC), New Delhi, India (UFR no. 62320), DST—SERB, New Delhi (Project No. EEQ/2017/000645), Rashtria Uchachatar Shiksha Abhiyan (RUSA), Government of Maharashtra, UGC-SAP Programme (F.530/16/DRS-I/2016 (SAP-II) Dt.16-04-2016) and DST-FIST (Project No. No. SR/FST/PSI-210/2016(C) dtd. 16/12/2016) for providing financial support, and Sabri Al-qutaibi for proofreading.

Author information

Authors and Affiliations

RUSA Center for Advanced Sensor Technology, Department of Physics, Dr. Babasaheb Ambedkar Marathwada University, Aurangabad, 431004, India
Theeazen AL-Gahouari, Pasha Sayyad, Gajanan Bodkhe, Nikesh Ingle, Manasi Mahadik & Mahendra Shirsat

Department Of Physics, Aden University, Aden, Yemen
Theeazen AL-Gahouari

Department of Electronics Engineering, Jawaharlal Nehru College of Engineering, Aurangabad, 431004, India
Sumedh Shirsat

Corresponding author

Correspondence to Mahendra Shirsat.

Additional information

Publisher's Note

Supplementary Information

Below is the link to the electronic supplementary material.

Supplementary file1 (DOCX 2455 KB)

Rights and permissions

About this article

Cite this article

AL-Gahouari, T., Sayyad, P., Bodkhe, G. *et al.* Controlling reduction degree of graphene oxide-based electrode for improving the sensing performance toward heavy metal ions. *Appl. Phys. A* **127**, 170 (2021). https://doi.org/10.1007/s00339-020-04199-6

Received	Accepted	Published
12 October 2020	07 December 2020	06 February 2021

DOI
https://doi.org/10.1007/s00339-020-04199-6

Share this article

Keywords

Reduced graphene oxide | Electrochemical reduction degree | Heavy metal ions detection | Differential pulse anodic stripping voltammetry | Oxygen-containing functional groups